

Spring 5-2018

Feasibility Study of a Multi-Purpose Aircraft Concept with a Leading-Edge Cross-Flow Fan

Stanislav Karpuk
Embry-Riddle Aeronautical University

Follow this and additional works at: <https://commons.erau.edu/edt>



Part of the [Aerospace Engineering Commons](#)

Scholarly Commons Citation

Karpuk, Stanislav, "Feasibility Study of a Multi-Purpose Aircraft Concept with a Leading-Edge Cross-Flow Fan" (2018). *Doctoral Dissertations and Master's Theses*. 399.

<https://commons.erau.edu/edt/399>

This Thesis - Open Access is brought to you for free and open access by Scholarly Commons. It has been accepted for inclusion in Doctoral Dissertations and Master's Theses by an authorized administrator of Scholarly Commons. For more information, please contact commons@erau.edu.

FEASIBILITY STUDY OF A MULTI-PURPOSE AIRCRAFT CONCEPT WITH A
LEADING-EDGE CROSS-FLOW FAN

A Thesis

Submitted to the Faculty

of

Embry-Riddle Aeronautical University

by

Stanislav Karpuk

In Partial Fulfillment of the

Requirements for the Degree

of

Master of Science in Aerospace Engineering

May 2018

Embry-Riddle Aeronautical University

Daytona Beach, Florida

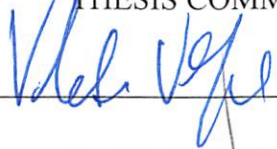
FEASIBILITY STUDY OF A MULTI-PURPOSE AIRCRAFT CONCEPT WITH A
LEADING-EDGE CROSS-FLOW FAN

by

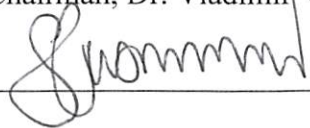
Stanislav Karpuk

A Thesis prepared under the direction of the candidate's committee chairman, Dr. Vladimir Golubev, Department of Aerospace Engineering, and has been approved by the members of the thesis committee. It was submitted to the School of Graduate Studies and Research and was accepted in partial fulfillment of the requirements for the degree of Master of Science in Aerospace Engineering.

THESIS COMMITTEE



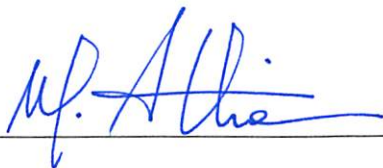
Chairman, Dr. Vladimir V. Golubev



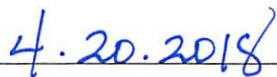
Co-advisor, Dr. Snorri Gudmundsson



Member, Dr. William Engblom



Graduate Program Coordinator, Dr. Magdy Attia



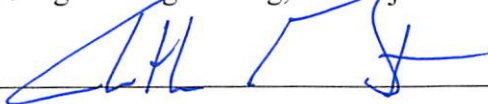
Date

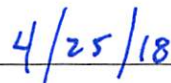




Dean of College of Engineering, Dr. Maj Mirmirani

Date





Vice Chancellor, Academic Support, Dr. Christopher Grant

Date

ACKNOWLEDGMENTS

I would like to thank Dr Gudmundsson and Dr Golubev for their knowledge, guidance and advising they provided during these two years of the program. I also would like to thank my committee member Dr Engblom for his advice and recommendations.

I also want to thank Petr and Marina Kazarin for their support, help and the opportunity to enjoy the Russian community for those two years.

This project would not be possible without strong computational power available in ERAU, so I would like to thank all staff and faculty who contributed to development and support of the VEGA cluster.

Finally, I would like to thank my infinite support and motivation – my mother and father. I would never achieve anything without you.

TABLE OF CONTENTS

LIST OF FIGURES	vi
SYMBOLS.....	x
ABBREVIATIONS	xii
ABSTRACT.....	xiii
1. Introduction.....	1
10.1. Review of the Cross-Flow Fan technology	1
10.2. Objective.....	4
2. Mission Definition and a baseline aircraft design.....	5
2.1. Mission Description and Aircraft Comparison	5
2.2. Mission Definition and Performance Requirements.....	5
2.3. Baseline Aircraft Configuration	7
3. Cross-Flow Fan Sizing and Aerodynamic Simulation.....	24
4. Airplane Modifications and performance comparison	34
5. CFF aircraft scaling analysis.....	41
6. Performance of the CFF airfoil with the opened bottom gap	47
7. Fan failure cases aerodynamic sensitivity studies	52
8. Conclusion	55
9. Recommendations	57
REFERENCES.....	58

A. The CFF airfoil velocity contours at cruise 60

B. The CFF airfoil velocity contours at cruise 62

LIST OF TABLES

Table 2.1. Regional transport aircraft data [IHS].....	6
Table 2.2. STOL aircraft mission requirements.....	7
Table 2.3. Airfoil competition analysis.....	11
Table 2.4. Maximum lift comparison between theoretical estimations and panel methods.	14
Table 2.5. Flow transition locations on the wing and the empennage.....	15
Table 2.6. Parasitic drag break-down.....	16
Table 2.7. Propeller Mach numbers at different altitudes.....	18
Table 2.8. Neutral point estimation comparison between theoretical estimations and panel methods (the distance is calculated from the nose).....	19
Table 2.9. Static stability coefficients of the baseline aircraft.....	19
Table 2.10. Dynamic stability characteristics of the baseline aircraft.....	19
Table 2.11. Take-off and landing performance.....	20
Table 2.12. Baseline aircraft weights.....	22
Table 2.13. Baseline aircraft geometric summary.....	23
Table 3.1. Time step sensitivity study.....	26
Table 4.1. EMRAX engines specifications.....	35
Table 4.2. Geometric configuration changes for the CFF aircraft.....	37

Table 4.3. Weights comparison.....	38
Table 4.4. Take-off performance comparison	39
Table 6.1. Mesh sensitivity analysis.....	51
Table 7.1. Aerodynamic comparison of the failed airfoil case to the baseline	54

LIST OF FIGURES

Figure 1.1 Cross-Flow Fan diagram	1
Figure 1.2. CFF applications as a propulsion system	2
Figure 1.3. A Goldschmied airfoil with an embedded CFF.....	2
Figure 1.4. Regional STOL jet concept	3
Figure 1.5. A Leading edge embedded CFF concept.....	3
Figure 1.6. Feasibility analysis work plan	4
Figure 2.1. Mission profile for a STOL-CFF aircraft concept.....	7
Figure 2.2. Baseline aircraft concept	7
Figure 2.3. NACA 65(4)221 airfoil	9
Figure 2.4. Airfoil competition drag polars	9
Figure 2.5. Baseline aircraft VSP model.....	10
Figure 2.6. NACA 65 ₄ -221with a Fowler flap ($\delta_f=25^0$)	10
Figure 2.7. Fowler flap trade study	10
Figure 2.8. Airfoil characteristics with deflected flaps	12
Figure 2.9. Baseline Aircraft lift curve	13
Figure 2.10. Airfoil CFD mesh	14
Figure 2.11. Baseline airplane drag polars.....	16
Figure 2.12. PT6A-135 engine.....	17

Figure 2.13. Baseline aircraft thrust and efficiency curves.....	17
Figure 2.14. The SURFACES VLM model.....	18
Figure 2.15. Climb performance	21
Figure 2.16. Payload-Range Diagram.....	21
Figure 2.17. Flight envelope	21
Figure 2.18. CG envelope. CG-locations are with respect to the aircraft nose.....	22
Figure 3.1. Modified airfoil with embedded CFF	24
Figure 3.2. Modified flapped airfoil with embedded CFF.....	24
Figure 3.3. CFF airfoil mesh.....	24
Figure 3.4. CFF airfoils computational meshes	25
Figure 3.5. Lift coefficient convergence history	26
Figure 3.6. Drag coefficient convergence history	26
Figure 3.7. Moment coefficient convergence history	27
Figure 3.8. Velocity distribution on the airfoil with the Fan in m/s	28
Figure 3.9. Convergence history of the.....	28
Figure 3.10. Convergence history of the CFF airfoil CFD solution	29
Figure 3.11. Velocity effect on lift coefficient.....	29
Figure 3.12. Velocity effect on drag coefficient	29
Figure 3.13. Velocity effect on moment coefficient	30

Figure 3.14. Velocity effect on torque coefficient	30
Figure 3.15. Velocity distribution on the airfoil with the Fan and the Fowler Flap in m/s	31
Figure 3.16. Lift curves for different airfoil configurations	32
Figure 3.17. Moment coefficients for different airfoil configurations.....	33
Figure 4.1. Gearbox and shaft layout for models 1 and 2.....	35
Figure 4.2. Model 3 Electrical system layout	36
Figure 4.3. Climb performance comparison	39
Figure 4.4. Payload-Range diagrams comparison	40
Figure 4.5. Flight envelope comparison.....	40
Figure 5.1. Take-off field length scaling analysis.....	42
Figure 5.2. Ground roll scaling analysis	43
Figure 5.3. Payload weight scaling analysis	44
Figure 5.4. Payload and take-off distance scaling as a function of wing loading.....	44
Figure 5.5. Cost function analysis results	45
Figure 6.1. Airfoil CFD far-field mesh	47
Figure 6.2. Airfoil CFD mesh	47
Figure 6.3. Velocity distribution at 0 deg AOA.....	48
Figure 6.4. Pressure coefficient distribution for the CFF wing at 0 deg AOA	48
Figure 6.5. Velocity contour for the CFF wing at 14 deg AOA	49

Figure 6.6. Pressure coefficient distribution for the CFF wing at 14 deg AOA	49
Figure 6.7. Lift curve for the CFF airfoil with a closed gap	50
Figure 6.8. Drag polar for these CFF airfoil with a closed gap	50
Figure 7.1. Lift curve for the CFF airfoil with a jammed airfoil	53
Figure 7.2. Drag polar for the CFF airfoil with a jammed fan.....	53
Figure 7.3. Convergence history of lift coefficient	54
Figure 7.4. Convergence history of drag coefficient	54
Figure 7.5. Velocity streamlines plot.....	54

SYMBOLS

α	Angle-of-attack
β	Angle-of-sideslip
τ	Torque
ω_N	Natural frequency
ω	Angular velocity
ζ	Damping ratio
b	Wing span
C_τ	Torque coefficient
C_D, C_d	Drag coefficient
C_{Df}	Skin friction drag coefficient
C_{Dmin}	Minimum drag coefficient
C_L, C_l	Lift coefficient
C_{La}	Lift curve slope
$C_{Lq}, C_{lp}, C_{Mq}, C_{Nr}$	Lift, roll, pitch, and yaw damping coefficients
$C_{L\delta e}, C_{l\delta a}, C_{M\delta e}, C_{N\delta r}$	Elevator, roll, pitch, and yaw power coefficients
$C_{l\delta r}, C_{N\delta a}$	Adverse yaw coefficients
C_{LminD}	Minimum drag lift coefficient
C_l	Rolling moment coefficient
$C_{l\beta}$	Dihedral effect
C_M, C_m	Pitching moment coefficient
C_{Ma}	Pitching moment-curve slope

$C_{N\beta}$	Weather vane stability coefficient
$C_{Y\beta}$	Sideslip force slope
c	Chord
H	Altitude
P	Power
q	Dynamic pressure
W_o	Gross weight
W_e	Empty weight
W_f	Fuel weight

ABBREVIATIONS

<i>AOA</i>	angle of attack
<i>APU</i>	Auxiliary power unit
<i>AR</i>	aspect ratio
<i>CFF</i>	Cross-Flow-Fan
<i>CFF airfoil</i>	Airfoil with embedded Cross-Flow Fan
<i>CG</i>	Center of gravity
<i>CRUD</i>	Cumulative Result of Undesired Drag
<i>(E)STOL</i>	(Extremely) short take-off and landing
<i>MAC</i>	Mean aerodynamic chord
<i>MTOW</i>	Maximum take-off weight
<i>RANS</i>	Reynolds-Averaged Navier-Stokes Equations
<i>RPM</i>	Revolutions per minute
<i>T-REX</i>	Hybrid mesh structure
<i>VTOL</i>	Vertical take-off and landing

ABSTRACT

Karpuk, Stanislav MSAE, Embry-Riddle Aeronautical University, May 2018. Feasibility Study of a Multi-Purpose Aircraft Concept with a Leading-Edge-Embedded Cross-Flow Fan.

A wing-embedded Cross-Flow Fan (CFF) was first proposed as an active flow control (AFC) device nearly 40 years ago. The CFF can be employed as a propulsion device as well as a high-lift system. This thesis research focuses on investigating the use of CFF as a high-lift device for an Extremely Short Take-off and Landing (ESTOL) aircraft. The wing-embedded CFF performance analysis is mostly addressed from an aerodynamic perspective and focuses on using such AFC technology in the conceptual aircraft design process. In particular, the design trade study of an aircraft featuring CFF as a high-lift device applied to a conceptual design of a medium-range multi-purpose aircraft is performed. A sensitivity analysis is employed to investigate the impact of the CFF on the aircraft weight, aerodynamics, stability and control, and flight performance. The aircraft design modifications are introduced to maximize the aircraft mission performance given the fan specifications and constraints. Results indicate a reduction of the take-off field length by 18% and 22% depending on the CFF system integration with the payload penalty of 14% and 17%, respectively. The aircraft ferry range is also decreased compared to the baseline aircraft design. The scaling analysis of the aircraft concept is performed to determine the potential market for such AFC technology. The results show that a light GA airplane or a small-to-medium size UAV could benefit more from the wing-embedded CFF compared to more heavy airplanes.

1. Introduction

1.1. Review of the Cross-Flow Fan technology

The Cross-Flow Fan (CFF) technology, first patented in 1893 by Mortier, is actively used for heating, ventilation, and air conditioning. The fan consists of three major parts: the inlet, the impeller with forward-curved blades located inside the housing consisting of

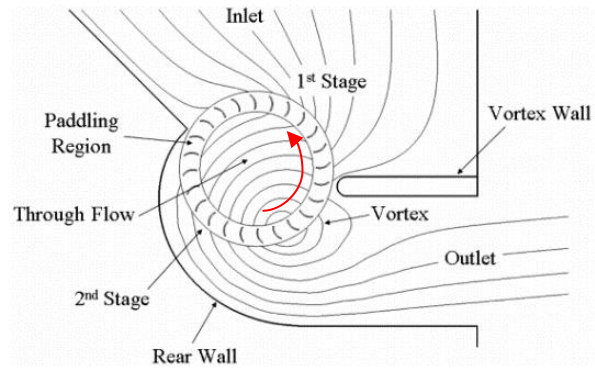
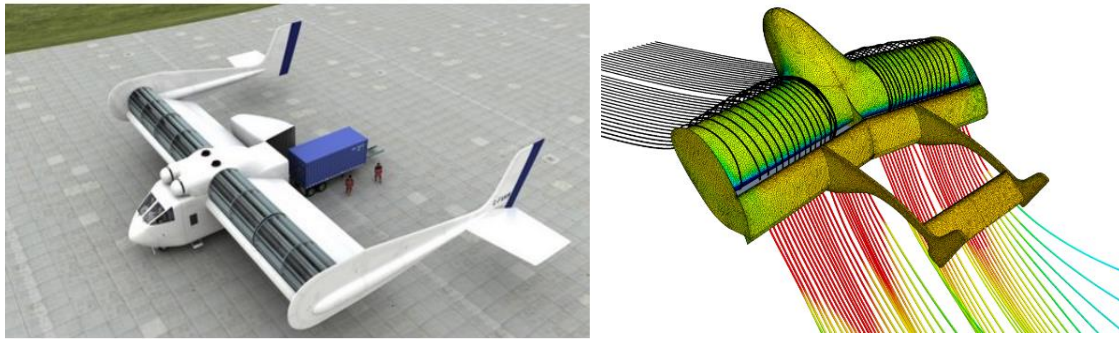


Figure 1.1 Cross-Flow Fan diagram

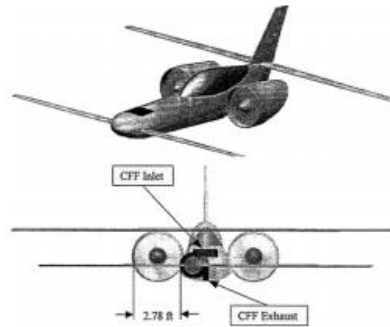
rear and vortex walls, and the outlet (Figure 1.1). For almost four decades, the fan has been discussed as a potential active high-lift and propulsion device for future aircraft. The applications of the CFF can be divided into two major groups: aircraft where the CFF is used as a propulsion system and the CFF used as an active flow control device.

The first group can be presented by the concepts shown in Figure 1.2. There, the FanWing concept designed by Peebles (Seyfang, 2012) is shown as a potential transport aircraft featuring the can across the wing span at its leading edge. The second concept studied and developed by Kummer and Dang (Kummer, 2006) Chawla (Chawla, 1984), Lin (Lin, 1986) and Nieh (Nieh, 1988) featured the aft-mounted CFF. The design featured a 34% thick (Figure 1.3(b)) airfoil as long as the separation was mitigated by the fan and a thick airfoil increased the aircraft internal volume. Numerical and experimental investigations showed significant increase in airfoil lift and increase of the stall angle of attack. In addition, Kummer demonstrated the thrust capabilities of the fan embedded close to the wing trailing edge by building a number of scaled UAV prototypes. Application of



a) FanWing

b) Propulsive Wing

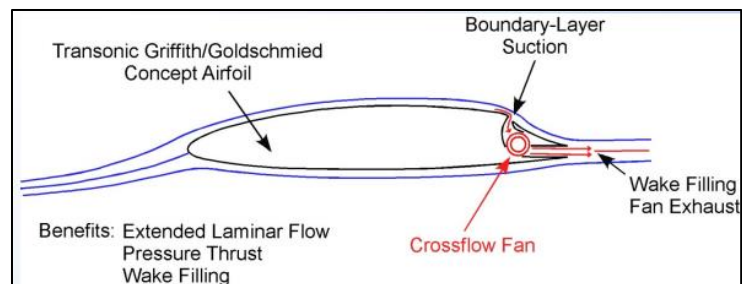


c) A light VTOL concept

Figure 1.2. CFF applications as a propulsion system

CFF as a VTOL device was studied by Gossett (Gossett, 2000) and included a conceptual design of a VTOL aircraft shown in Figure 1.2 (c).

In the second group, the CFF is used as an active flow control device for either cruise flight or take-off and landing. Application of CFF to a commercial aircraft was studied by Kramer et al. (Kramer, 2016) and showed a promising result. It was determined that an optimized Goldschmied wing with the fan embedded at the trailing edge for the transonic

**Figure 1.3.** A Goldschmied airfoil with an embedded CFF

commercial aircraft could reduce fuel consumption comparing to Boeing SUGAR aircraft by 12% percent due to an extended laminar boundary layer provided by the CFF suction. Figure 1.3 shows the Goldschmied airfoil with



Figure 1.4. Regional STOL jet concept

the embedded CFF. The research on using CFF as a high-lift device was conducted by Goland et al (Goland, 2009) and Phan (Phan, 2015). Goland studied a potential application of the CFF configuration proposed by Kummer for a regional jet aircraft. Although, the fan was not optimized, preliminary results

showed a potential of the the CFF to be used as a high-lift device. Phan, however, investigated a different configuration, with CFF embedded into the leading edge of the wing, as shown in Figure 1.4. He applied his results to examine flight performance data based on Piper PA-18 aircraft. The

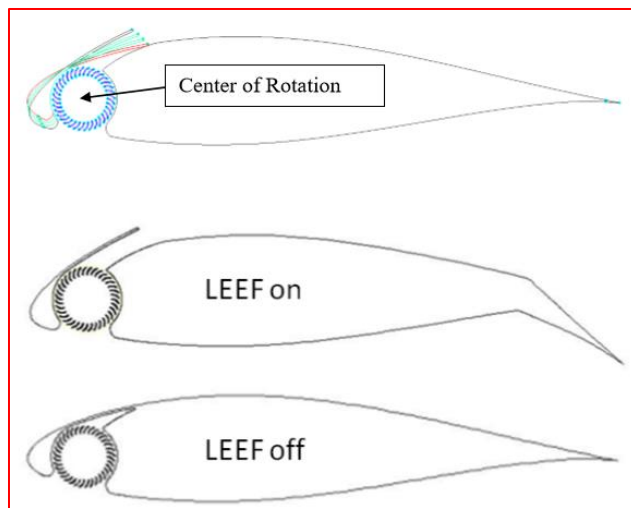


Figure 1.5. A Leading edge embedded CFF concept

results demonstrated reduction of the take-off run by 50%. In addition, three-dimensional CFD analysis was performed on a wing featuring a cross-flow fan embedded along the entire span.

1.2. Objective

While significant work has been done regarding the CFF physics and its aerodynamic performance as part of the aircraft wing design, no multi-disciplinary feasibility analysis of the CFF-based high-lift technology was performed in the past. The current work implements such feasibility study of the wing-embedded CFF technology and its influence on the conceptual design of a multi-purpose ESTOL aircraft. The feasibility analysis will be decomposed into 3 parts. In the first part, the design mission, requirements and constraints will be established and the baseline aircraft will be designed. The second part will describe the procedure and introduces the methods and tools required to perform a feasibility analysis to develop a design featuring the CFF. The third part will demonstrate comparison between the baseline aircraft design and its modified version with the embedded CFF and discuss benefits and drawbacks of the technology.

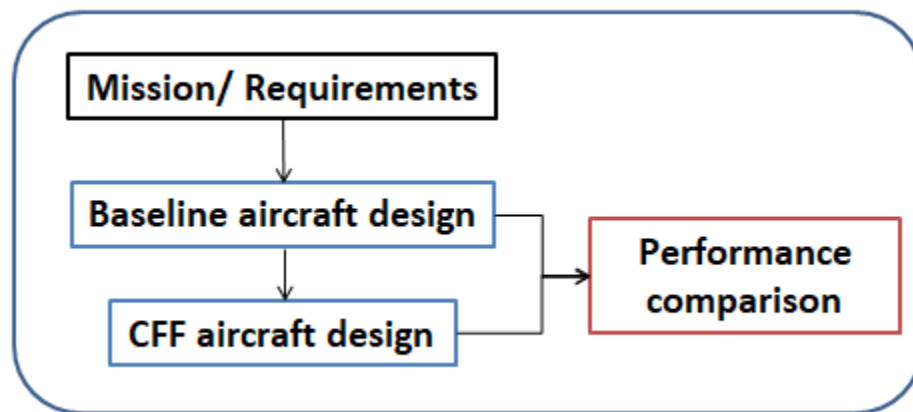


Figure 1.6. Feasibility analysis work plan

2. Mission Definition and a baseline aircraft design

2.1. Mission Description and Aircraft Comparison

The design requirements for STOL aircraft include short take-off and landing distances on different runway profiles and arrival to the destination point as quickly as possible. On the other hand, the requirements of a short take-off and landing distance and high-speed flight are contradictory if one of the parameters is maximized. For instance, helicopters may take off instantly from any surface due to their VTOL features, but the helicopter's speed is significantly limited due to the limitations of its flight physics. On the other hand, modern regional aircraft may show much stronger speed characteristics compared to helicopters, but they lack the ability to take off and land on an unprepared runway with the shortest possible distance. Thus, combining VTOL and high-speed flight is a challenging task due to the complexities involved in the combination of two requirements: minimizing take-off and landing distances while maintaining strong cruise performance. As a compromise, we consider the CFF-based ESTOL approach that would preserve strong cruise performance characteristics of the proposed wing design.

2.2. Mission Definition and Performance Requirements

The mission profile and performance requirements are based on the idea of matching the aircraft performance of a typical General Aviation transport propeller aircraft and maximizing its STOL capabilities. A number of aircraft were studied with averaged performance characteristics shown in Tables 2.1. Based on the obtained data, the mission requirements were determined, as presented in Table 2.2.

Table 2.1. Regional transport aircraft data [IHS]

	Gross Weight (lb)	Payload Weight (lb)	Empty weight (lb)	Max Cruise speed (KTAS)	Rate-of-Climb (fpm)	Power loading (lb/hp)	Wing loading (lb/ft²)	Max Power (SHP)
IAI Arava	15000	4080	8816	176	1290	10.00	31.90	1500
CASA-212	16975	4080	8333	200	1630	9.43	38.49	1850
DHC-6	12500	3230	6881	170	1600	8.33	29.76	1500
Dornier 228	14550	3230	8243	223	1870	10.17	42.30	1552
Ev-55	10141	1530	5860	220	-	9.39	39.77	1070
Y-12	11684	2890	6621	177	1595	9.42	31.67	1240
Average	14142	3502	7779	189.2	1597	9.47	35.65	1452

The take-off and landing distances were not quantitatively specified, but the ground run must be minimized as much as possible. The mission profile shown in Figure 2.1 represents a typical IFR mission with additional 100nmi - 120nmi for divert maneuver.

Table 2.2. STOL aircraft mission requirements

Maximum Payload (lb)	4200
Rate-of Climb (fpm)	≥ 1600
Max Cruise speed (KTAS)	≥ 200
Mission profile	VFR and IFR

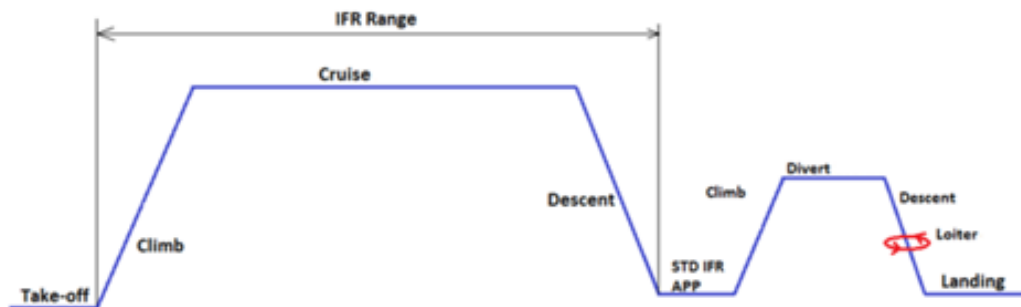


Figure 2.1. Mission profile for a STOL-CFF aircraft concept

2.3. Baseline Aircraft Configuration

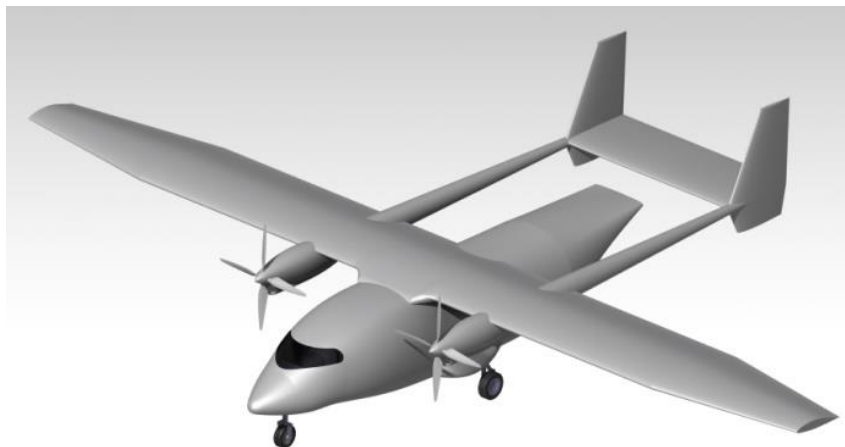


Figure 2.2. Baseline aircraft concept

To evaluate feasibility of an airplane featuring the CFF technology, a baseline aircraft model similar to existing airplane of a given class must be designed. Then, a modified airplane with embedded CFF will be compared to the baseline model to study benefits and drawbacks of the CFF technology. The baseline aircraft configuration with conventional high-lift devices was designed to match the mission requirements and take potential modifications for the CFF integration into account. The airframe was designed using theoretical and semi-empirical approaches as well as design tools including SURFACES [SURFACES] and MATLAB for stability and control, Open Vehicle Sketch Pad (OpenVSP) (Hahn, 2013), and CATIA for geometric modeling. Cruise speed and altitude were determined based on performance of the competitors and were equal to 160 KCAS at 10000 ft.

The aircraft design of the baseline model has one constraint: the wing shape should be designed such that the embedded fan would have a uniform diameter along the wing's span. This constraint is based on two-dimensional CFD analysis of the CFF airfoil which limits tapering opportunities due to changes in flow coefficient and, as a result, aerodynamics of the wing. A three-dimensional analysis of the tapered wing with embedded CFF will be a subject of the future studies.

The baseline aircraft features a high-wing configuration to make maneuvering around the aircraft easier and have higher ground

2.3.1. Aerodynamics

Airfoil selection had a number of requirements selection criteria:

- The airfoil should have a large thickness to be able to embed the CFF

- The airfoil should feature NLF with extended laminar flow region
- The airfoil selection was based on the aircraft cruise and climb performance as long as the high AOA behavior.

Based on the criteria shown above, three airfoils were chosen as the main competitors. The airfoil that scores the most points for particular design criteria is the best one. The results of the trade studies are shown in Table 2.3. Based on the trade studies, both NACA 65₄-221 and NACA 66₄-221 show superior performance compared to the NACA 63₄-221.

However, drag coefficient at higher angles of attack has a substantially larger magnitude for the NACA 66₄-221 compared to the NACA 65₅-221, as shown in Figure 2.4. Consequently, NACA 65₄-221 was chosen for the current wing design.

The wing planform has a semi-tapered configuration with a constant chord section up to 67% of span to embed the fan, with the taper ratio of 0.5. The baseline clean configuration's lift parameters were estimated using methods of Raymer

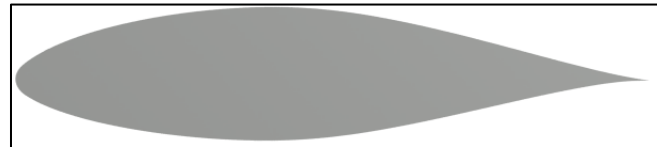


Figure 2.3. NACA 65(4)221 airfoil

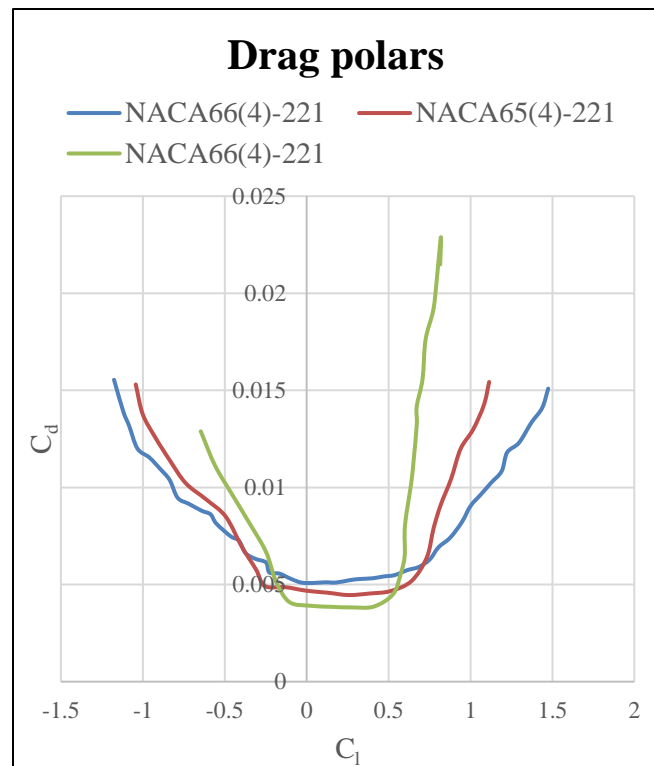


Figure 2.4. Airfoil competition drag polars

(Raymer, 2012) and Torenbeek (Torenbeek, 1982) and were validated with VLM VSPAERO package (Hahn, 2013). Figure 2.5 shows the VSP model of the baseline aircraft.

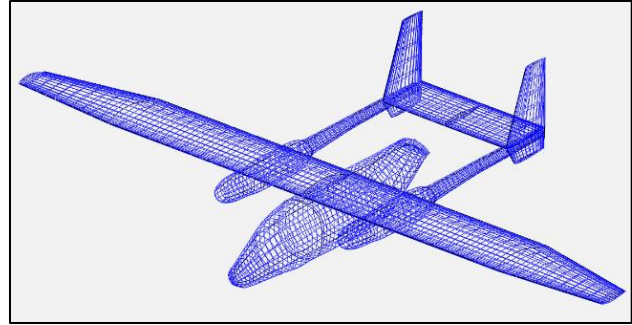


Figure 2.5. Baseline aircraft VSP model

The effect of high-lift devices was estimated using a method of Torenbeek (Torenbeek, 1982). A single-slotted Fowler flaps were used. Flap-to-chord ratio was equal to 30%, and effective (with account for engine and fuselage segments) flap-to-span ratio was equal to 50%, which satisfied aileron power to satisfy roll-rate requirements presented in FAR Part 23 (CFR, 2017). In addition, a sample study of conventional airfoil with Fowler flaps was performed using CFD. Pointwise [Pointwise] and ANSYS Fluent [ANSYS] software were used to generate the meshes and perform the simulations.

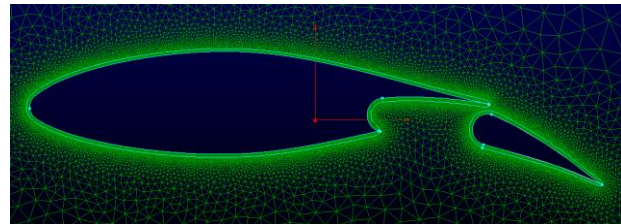


Figure 2.6. NACA 654-221 with a Fowler flap ($\delta_f=25^\circ$)

The grids are unstructured with hybrid-mesh T-REX structure used for the boundary layer. Average mesh size for each airfoil is 80000 cells, with Y^+ is equal to 1. Far field is located 100 chord lengths away from the airfoil surface to satisfy the far-field boundary condition.

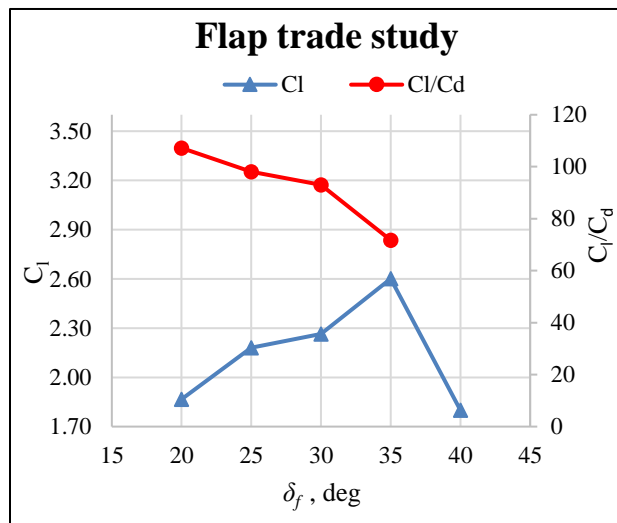


Figure 2.7. Fowler flap trade study

Table 2.3. Airfoil competition analysis

Parameters\Airfoil	Characteristics			Score		
	NACA63 ₄ -221	NACA65 ₄ -221	NACA66 ₄ -221	NACA63 ₄ -221	NACA65 ₄ -221	NACA66 ₄ -221
Thickness (%)	21	21	21			
C_{l0}	0.16	0.16	0.15	1	1	
AOA for $C_l=0$	-1.5	-1.6	-1		1	
C_{lmax}	1.45	1.48	1.5			1
AOA for C_{lmax}	18	20	19		1	
C_{dmin}	0.0053	0.0045	0.0037			1
C_l at C_{dmin}	0.2	0.28	0.2	1		1
$(C_l/C_d)_{max}$	116.7	100	125			1
C_l of $(C_l/C_d)_{max}$	0.7	0.6	0.5			1
Cruise C_m	-0.05	-0.025	-0.026		1	
Drag bucket start at C_m	-0.2	-0.2	-0.1			
Drag bucket end at C_m	0.6	0.6	0.5			
C_l Climb in drag bucket	Y	Y	N	1	1	
C_l Cruise in drag bucket	Y	Y	Y	1	1	1
				4	6	6

Unsteady RANS with Transition SST turbulence model [ANSYS] was used to ensure convergence of the solution at high angles of attack when the flow begins to separate.

Several flap deflections were tested to investigate the effect of the flap on lift and drag. The flapped NACA 65(3)-221 airfoil mesh is shown in Figure 2.6. Figure 2.7 shows the flap trade study. The latter indicates that the Fowler flap stalls at the deflection of 40° while the maximum possible lift is achieved at 35° . To combine benefits of the lift enhancement of the flap and have less drag penalty, the take-off flap deflection of 25° was considered. For landing, the deflection of 35° with maximum lift was chosen.

Figure 2.8 shows lift curves for the flapped airfoil configurations and the clean benchmark airfoil compared to the experimental data from Abbot (Abbot, 1959). The

benchmark data shows high accuracy of lift compared to the experimental data. Flapped airfoils show general trends typical to the airfoils featuring single-slotted flaps: the lift-curve slope and the zero AOA lift coefficients are both increased, and stalling of the flapped airfoils happens at lower angles of attack compared to the clean configuration.

Two-dimensional lift obtained from CFD at 0 degrees AOA and maximum AOA were transformed

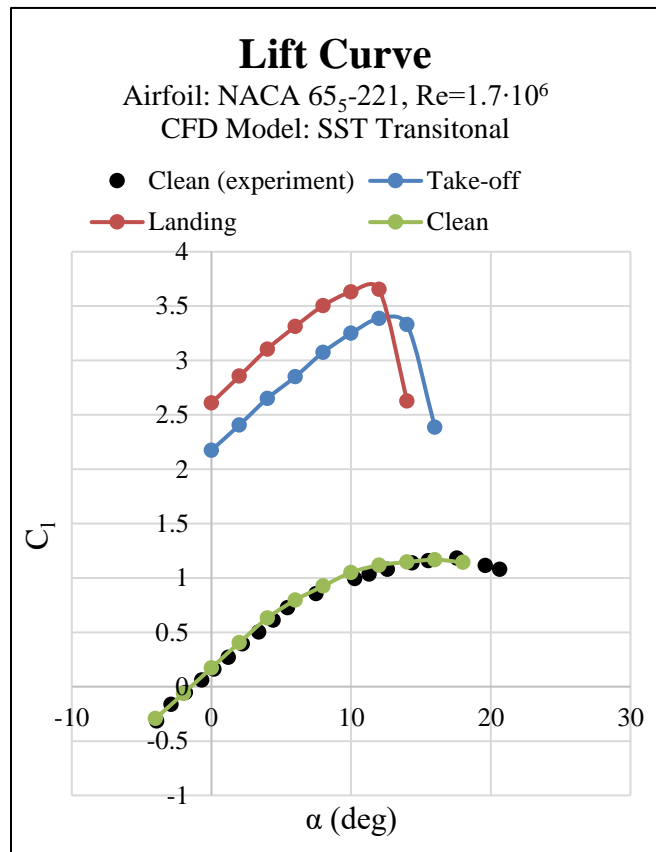


Figure 2.8. Airfoil characteristics with deflected flaps

using semi-empirical methods from Torenbeek (Torenbeek, 1982). Both for the clean and flapped configurations, Figure 2.9 shows good comparison between the semi-empirical lift estimates, panel methods, and CFD results. Furthermore, Table 2.4 presents a good agreement between theoretical estimations and results from the panel methods for stalling characteristics.

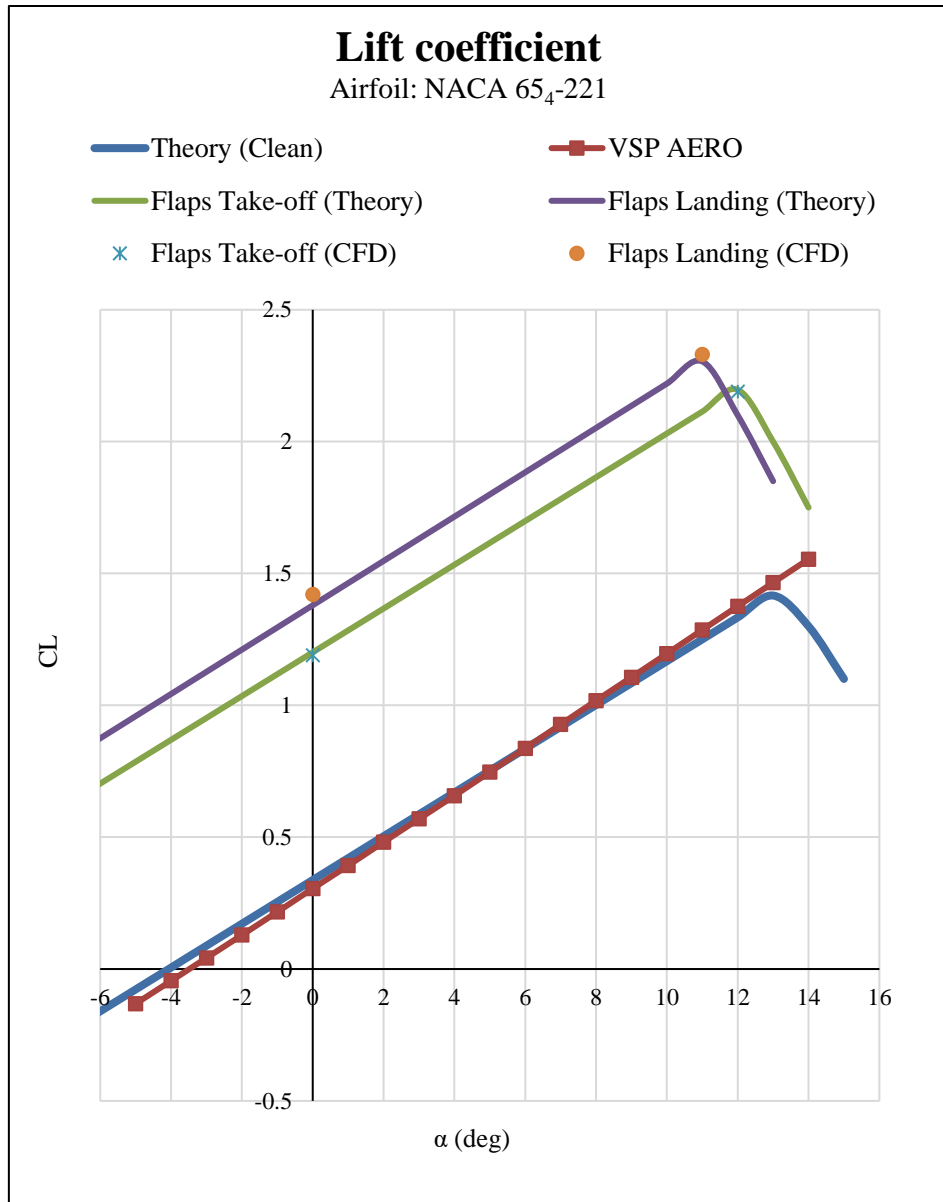


Figure 2.9. Baseline Aircraft lift curve

Table 2.4. Maximum lift comparison between theoretical estimations and panel methods.

	Maximum angle-of-attack (deg)	Maximum lift coefficient
Theory	13	1.43
VSPAERO	13	1.47

A modified drag model was implemented to give more accurate drag estimation and is represented by

$$C_D = C_{Dmin} + \frac{(C_L - C_{LminD})^2}{\pi eAR} \quad (1)$$

where C_{Dmin} is minimum drag coefficient and includes parasite, pressure, and miscellaneous drag while C_{LminD} is lift coefficient at minimum drag obtained from OpenVSP panel code [Hahn, 2013] at a preliminary stage.

Skin-friction drag was estimated using a method of Young (Young, 1989). To effectively utilize the method, transition of the flow at the root and the tip of the surface is required. Pointwise grid generator and ANSYS FLUENT CFD packages were used to determine the boundary- layer transition point. Figure 2.10 shows an example C-grid generated for the wing root airfoil. The mesh for each airfoil consist of 15000-25000 points with Y^+ equal to 1. Far field is located 100 chord length away from the airfoil surface which ensures the far-field boundary

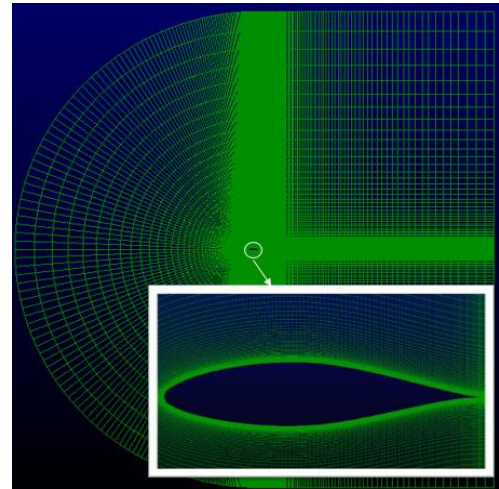


Figure 2.10. Airfoil CFD mesh

condition. Steady RANS with Transitional SST model was used. Table 4 shows transition locations for the aircraft wing and empennage.

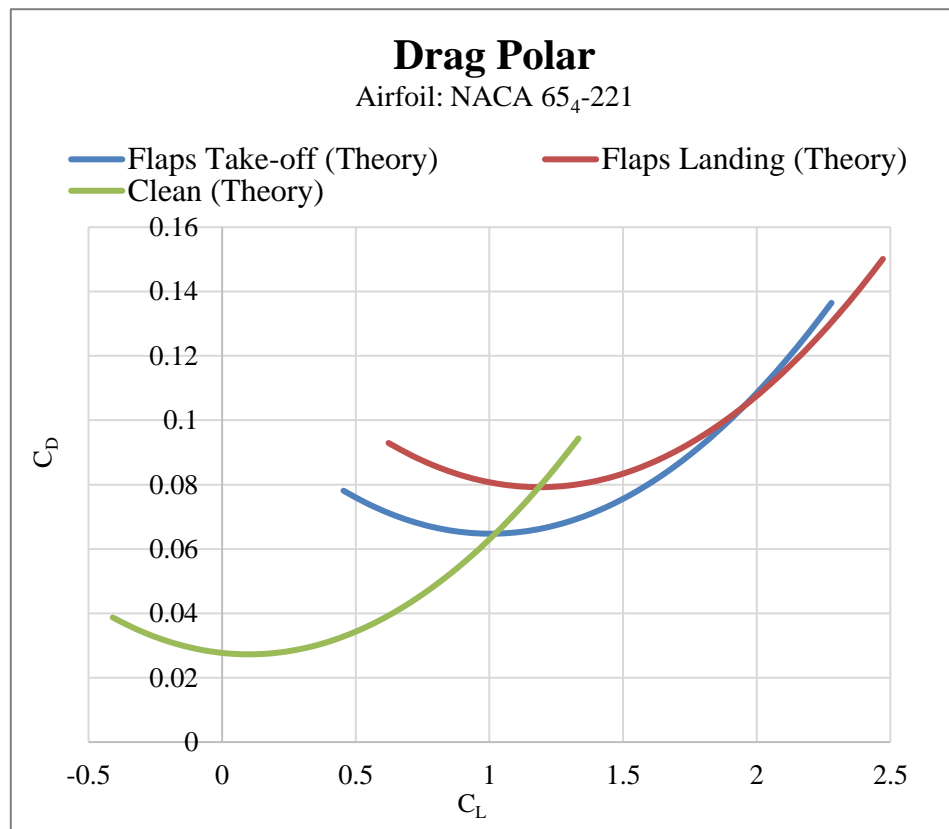
Fuselage parasite drag assumed a fully turbulent flow. In addition, the base drag was calculated using Torenbeek. To include the effect of drag due to extra components not included in the conceptual design stage, the value of CRUD was assumed at 25% (Gudmundsson, 2013) of total minimum drag coefficient. The drag components breakdown is shown in Table 2.5.

Table 2.5. Flow transition locations on the wing and the empennage

Aircraft component	Airfoil	Transition location (% chord)
Wing root top surface	NACA 65 ₄ -221	10
Wing root bottom surface	NACA 65 ₄ -221	10
Wing tip top surface	NACA 65 ₄ -221	19
Wing tip bottom surface	NACA 65 ₄ -221	16
Horizontal tail root	NACA 0012	45
Horizontal tail tip	NACA 0012	45
Vertical tail root	NACA 0010	50
Vertical tail tip	NACA 0010	50

Table 2.6. Parasitic drag break-down

	C_{Df}	Contribution (%)
Wing	0.0135	53.8
Horizontal tail	0.0012	4.78
Vertical Tail	0.0016	6.37
Fuselage	0.0041	16.33
Tail Booms	0.0026	10.36
Miscellaneous	0.0020	7.97
CRUD (%)	25.00	
Total	0.0326	100.00

**Figure 2.11.** Baseline airplane drag polars

2.3.2. Propulsion

For the given speed and altitude, the turboprop engines show the most efficient performance for the selected aircraft configuration. Based on performance results, two Pratt & Whitney PT6A-135 with 750 SHP each with a constant speed



Figure 2.13. PT6A-135 engine

propeller and a thrust reversal feature were chosen. The propeller diameter is equal to 90 in to maximize the thrust generation and avoid critical Mach numbers at the blade tips. Table 2.7 shows the tip Mach numbers for important flight altitudes. Key engine parameters required for the design were obtained from Jane's (IHS). The engine thrust

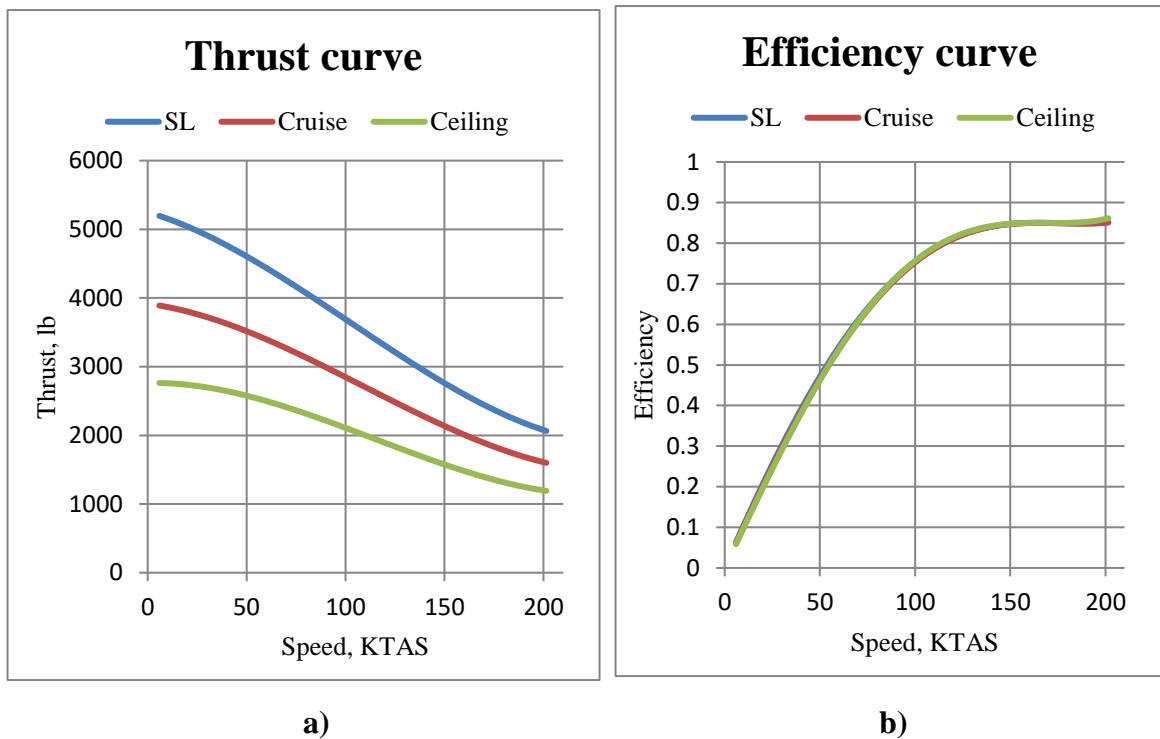


Figure 2.12. Baseline aircraft thrust and efficiency curves

performance data based on the cubic spline method (Gudmundsson, 2013)) and the efficiency plots are shown in Figure 2.13.

Table 2.7. Propeller Mach numbers at different altitudes

Altitude	Tip Mach number
Sea Level	0.65
Cruise	0.67
Ceiling	0.71

2.3.3. Stability & Control

Both static and dynamic stability calculations were performed to determine stability characteristics of the aircraft and its handling qualities. Horizontal and vertical tails were sized such that the desired CG range

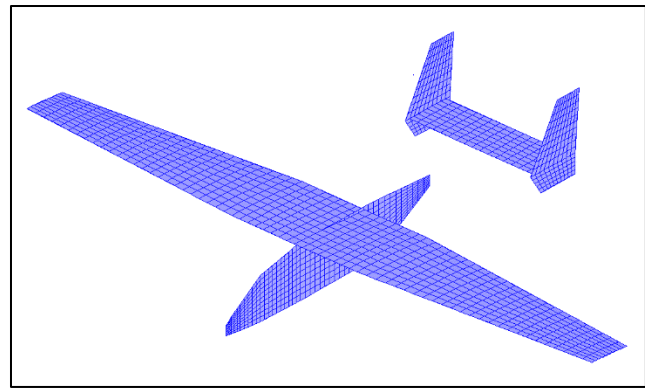


Figure 2.14. The SURFACES VLM model

discussed below was satisfied and the rudder deflection was not excessive in case of a single engine failure. Theoretical estimation of the static stability was performed using methods presented by Raymer (Raymer, 2012) and Nelson (Nelson, 1998). The neutral point obtained with theoretical approach was validated using SURFACES VLM software. The corresponding model of the airplane is shown in Figure 2.14. Table 2.8 presents neutral point comparison between theory and panel methods. Static stability derivatives for the baseline aircraft are shown in Table 2.9. In addition, dynamic stability of the aircraft using MATLAB-SIMULINK 6- DOF model was analyzed. Results presented in Table 2.10 were

compared to handling qualities requirements by FAR Part 23. All modes satisfy Level 1 requirements.

Table 2.8. Neutral point estimation comparison between theoretical estimations and panel methods (the distance is calculated from the nose)

	Neutral point loc-n from the nose (ft)	% Mean Aerodynamic Chord
Theory	15.11	46
SURFACES	15.06	45

Table 2.9. Static stability coefficients of the baseline aircraft

Longitudinal	Value	Lateral	Value
$C_{L\alpha}$	4.94	$C_{N\beta}$	0.132
$C_{L\delta e}$	0.568	$C_{N\delta r}$	-0.114
$C_{M\alpha}$	-0.625	$C_{N\delta a}$	-0.015
C_{Mq}	-9.06	$C_{l\beta}$	-0.052
$C_{M\delta e}$	-1.95	$C_{l\delta a}$	0.219
		$C_{l\delta r}$	0.024
		C_{lp}	-0.601

Table 2.10. Dynamic stability characteristics of the baseline aircraft

Mode	Parameter	MIL-STD Cat. B Level	Baseline
Short Period	Damping	$0.30 < \zeta_{SP} < 2.00$	0.44
	Natural frequency (rad/s)	$1.10 < \omega_{NSP} < 6.00$	3.44
Phugoid	Damping	$\zeta_{PH} > 0.04$	0.322
Dutch Roll	Damping	$\zeta_{DR} > 0.08$	0.145
	Natural frequency (rad/s)	$\omega_{NDR} < 4.00$	2.27

2.3.4. Performance

The Aircraft performance was estimated using methods presented by Gudmundsson (Gudmundsson, 2013). With conventional high-lift devices, the take-off ground run was estimated at 1212 ft on dry concrete, and take-off distance with 50 ft obstacle was equal to 1912 ft. The landing distance with 50 ft obstacle was equal to 1498 ft. Baseline aircraft take-off and landing performance is summarized in Table 2.11.

Table 2.11. Take-off and landing performance

Description	Value
Take-off ground run (ft)	1212
Take-off field length (ft)	1912
Landing approach distance (ft)	659
Flare distance (ft)	113
Free-roll distance (ft)	197
Breaking distance (ft)	576
Total landing distance (ft)	1498

The climb performance diagram presented in Figure 2.15 shows the maximum rate-of climb of 1684 fpm at sea-level and 1067fpm at cruise altitude, which is comparable to general aviation aircraft of the same class. Cruise performance can be described with flight envelope and a payload-range diagram. The payload-range diagram shown in Figure 2.16 demonstrates the ferry range of 1170 nmi at maximum range speed and 901 nmi at maximum speed. Figure 2.17 shows the flight envelope where maximum flight speed is equal to 201 KTAS cruise altitude.

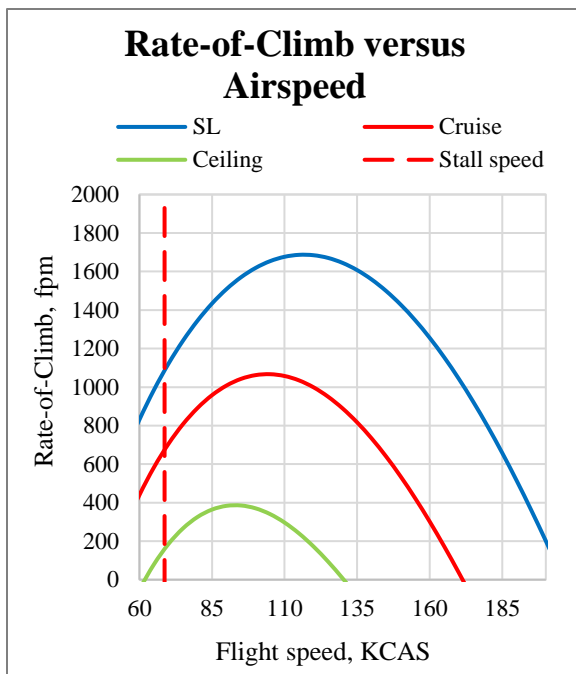


Figure 2.16. Climb performance

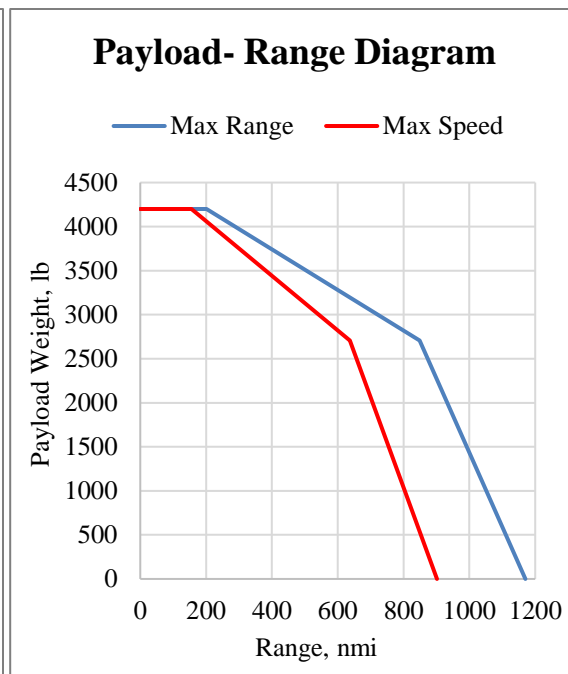


Figure 2.15. Payload-Range Diagram

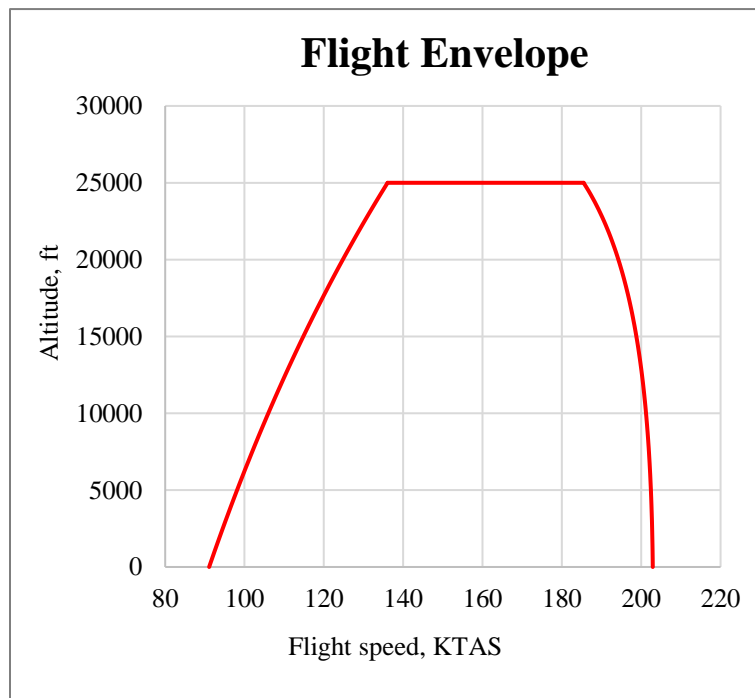


Figure 2.17. Flight envelope

2.3.5. Weights and Balance

Empty weight estimation was performed using the methods of Raymer, Torenbeek, Nicolai (Nicolai, 2010), and Niu (Niu, 1988) to determine the averaged weights of key aircraft components. Table 2.12 presents final baseline aircraft weights. Based on the most forward and aft positions of the CG depending on payload location and weight, the fuel weight, and the horizontal tail sizing, the CG envelope was created and is demonstrated in Figure 2.18. The baseline concept demonstrates cg range of 16% MAC which is comparable to general aviation aircraft.

Table 2.12. Baseline aircraft weights

Maximum Take-off Weight (lb)	16187
Maximum Landing Weight (lb)	15701
Maximum Fuel Weight (lb)	3457
Payload Weight (lb)	4200
Empty Weight (lb)	9684

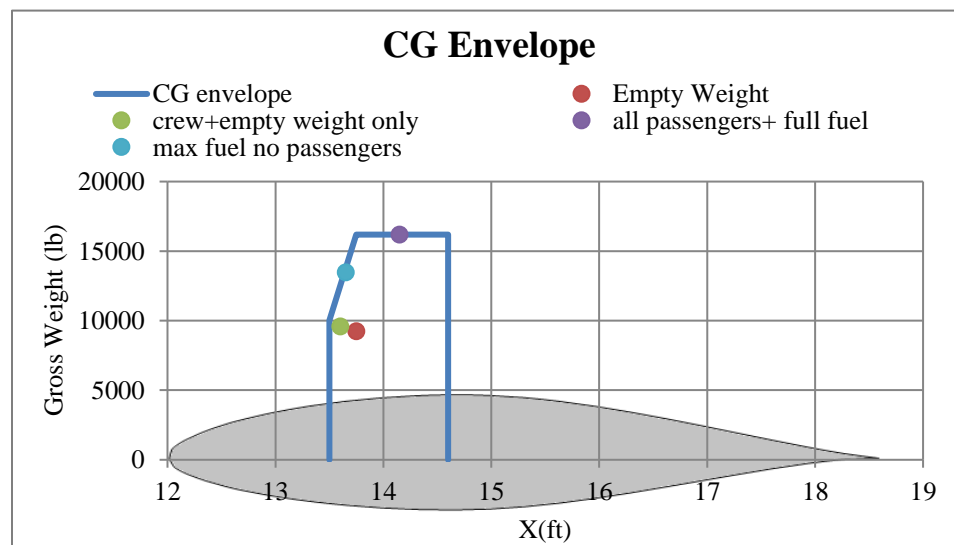


Figure 2.18. CG envelope. CG-locations are with respect to the aircraft nose

6. Geometric Summary

Table 2.13 shows the resulting geometric properties of the wing and tails for the baseline configuration.

Table 2.13. Baseline aircraft geometric summary

Baseline Concept			
Length (ft)	42.55		
Height (ft)	14.25		
	Wing	Horizontal Tail	Vertical Tail
Span (ft)	66	15.00	9
AR	10.00	3.50	4.20
Root Chord (ft)	7.20	5.50	5.50
Taper Ratio	0.50	1.00	0.50
Incidence (deg)	3.00	-2.00	0.00
LE Sweep (deg)	3.45	0.00	20.00
Volume coefficient		0.67	0.067

3. Cross-Flow Fan Sizing and Aerodynamic Simulation

To perform a trade study of the aircraft with the wing-embedded CFF as a high-lift device, initial fan configuration and its location must be determined. The fan concept of Kummer [1] was used as a baseline configuration, with the fan positioned at the wing leading edge.

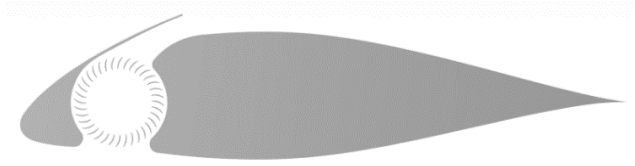


Figure 3.2. Modified airfoil with embedded CFF

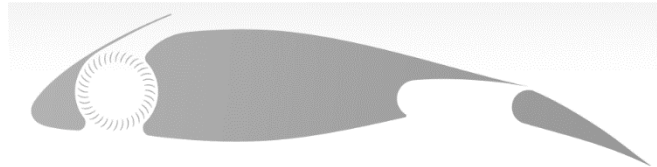


Figure 3.1. Modified flapped airfoil with embedded CFF

The airfoil chord length is 5.6 ft, which was based on initial mean aerodynamic chord of the airplane. The fan is located at 17% chord, with the fan diameter of 0.82 ft. The main spar is then located at 25% chord. The blade-to-diameter ratio is equal to 0.75, with 36 blades employed in the fan. The fan gap between the blades and the walls is equal to 5%.

The slot of the fan rotates 15 degrees about the fan center for the take-off and landing, and it closes during the flight. In addition, to maximize take-off performance, a Fowler flap was applied. Figures 3.1 and 3.2 show the airfoils with and without the Fowler flap.

The computational domain for the airfoil without the flap was generated

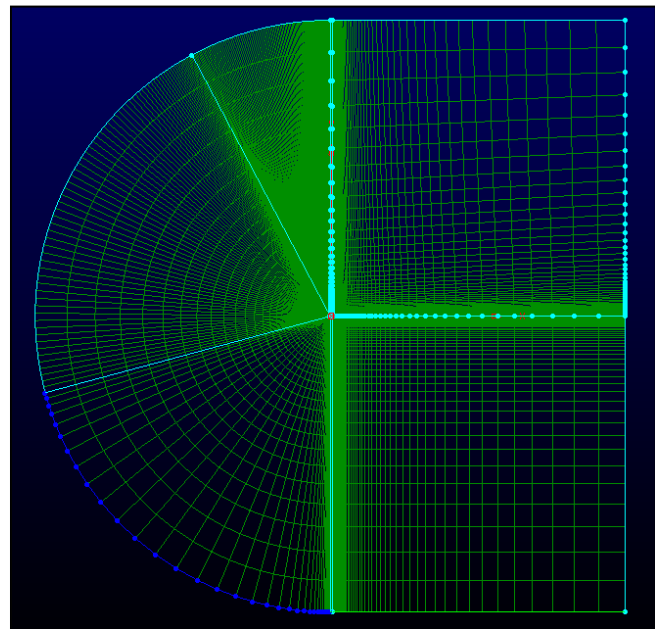


Figure 3.3. CFF airfoil mesh

using a mixed mesh with the unstructured portion inside the fan surrounded by a structured mesh around the airfoil. To simplify generation of the mesh for the flapped airfoil, a fully unstructured mesh with T-REX (Pointwise) structure was used. Figures 3.3 and 3.4 show the computational domains of the airfoils generated in Pointwise. Y^+ is equal to 1 to resolve the boundary layer behavior and far field is located 100 chord length away from the airfoil surface, which ensures the proper implementation of the far-field boundary condition. To ensure accuracy of the solution with rotating fan, an appropriate time step was chosen based on sensitivity studies. The airfoil without the flap was tested for different time step. Results presented in Table 3.1 show that the time step of $10E-4$ is sufficient to accurately capture the physics of the rotating fan. For the airfoil with the Fowler flap, maximal rotation of 30 degrees ensures attachment of the flow from the fan and maximizes lifting characteristics.

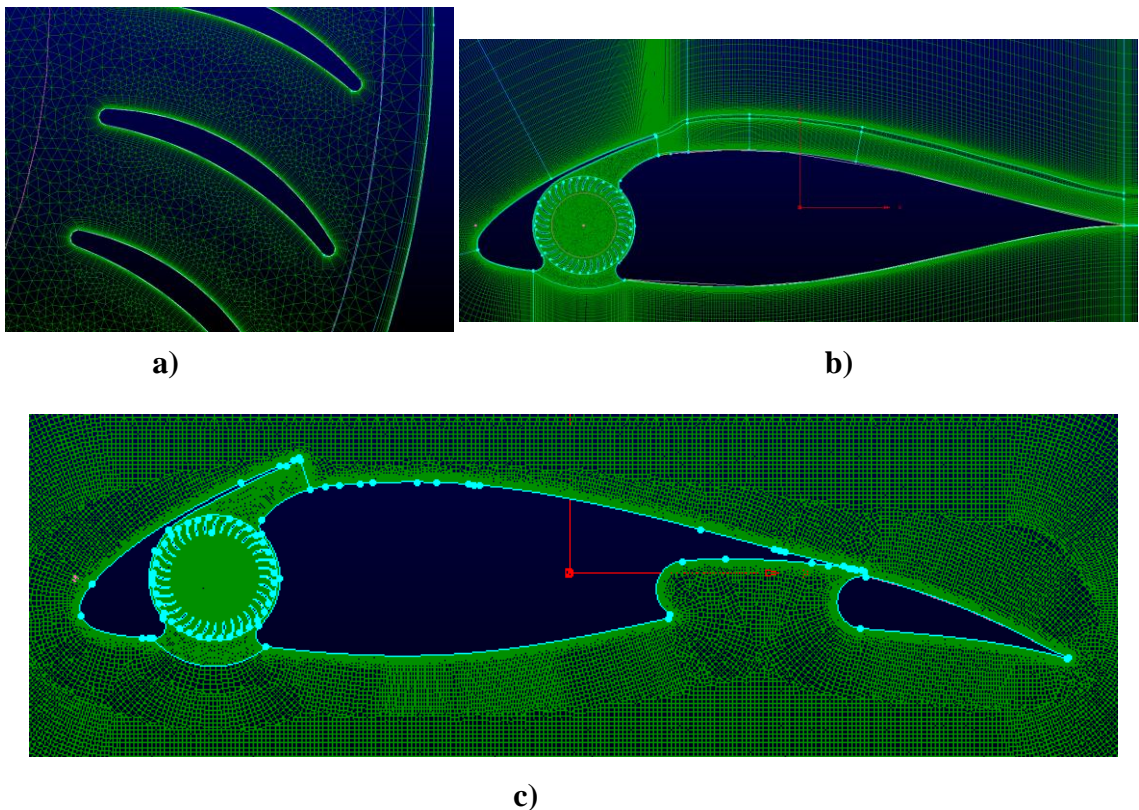


Figure 3.4. CFF airfoils computational meshes

Based on the analysis of turbulence models presented by Phan, the 2nd-order accurate unsteady RANS with Spalart-Allmaras turbulence model was used to calculate lift, drag, moment about the quarter chord, and torque coefficients. Semi-empirical methods of Torenbeek were implemented to transform the two-dimensional data into three-dimensional one. Solution convergence is achieved when aerodynamic coefficients of the airfoil become nearly constant. Figures 3.5-3.7 show examples of the convergence time history from the numerical solution for the CFF airfoil. The example velocity distribution on the airfoil is shown in Figure 3.8.

Based on results presented by Phan, CFF airfoil substantially increases the maximum angle of attack and increases the lift coefficient due to the difference in dynamic pressure on the airfoil as a result of the blowing effect of the fan. In addition, the lift curve slope remains constant over a longer

Table 3.1. Time step sensitivity study

Time step	C_l	C_d	C_τ	C_m
0.0005	1.7	-0.65	0.14	-0.36
0.0001	1.55	-0.66	0.14	-0.36
0.00005	1.55	-0.72	0.14	-0.36

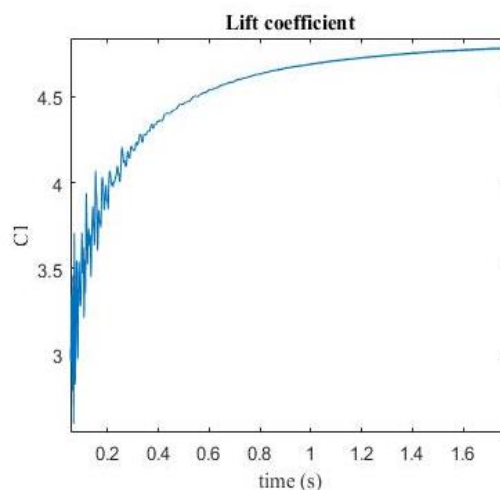


Figure 3.5. Lift coefficient convergence history

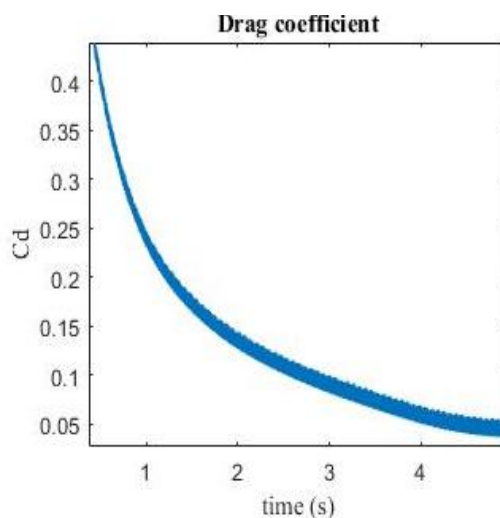


Figure 3.6. Drag coefficient convergence history

range of AOA compared to conventional airfoils. Therefore, the simulations were performed for -15, 0, and 16 degrees AOA as long as the take-off rotation angle is determined by the sections of the wing that do not feature the Fan.

The fan RPM value determines the power required for the engine to run the device. In addition, the span of the fan also affects the power required for the fan. The airfoil without the flap was tested to determine the best angular velocity and power required for the fan.

The angular velocities of 200 rad/s, 400 rad/s, 600 rad/s, and 800 rad/s were tested for the airfoil at 0 degrees AOA and free stream velocity of 15 m/s. The fan torque per unit span is defined by

$$\tau/b = C_{\tau} q_{\infty} c^2 \quad (2)$$

where q_{∞} is the dynamic pressure, and C_{τ} is the torque coefficient obtained from CFD analysis.

Then, the fan power per unit span is thus

$$P/b = \tau \omega / b \quad (3)$$

where ω is the angular velocity. The power obtained for the airfoil has units per unit span, so the total power is found by multiplying the power by required span of the wing. Results of the Fan RPM trade study is shown in Figure 3.9.

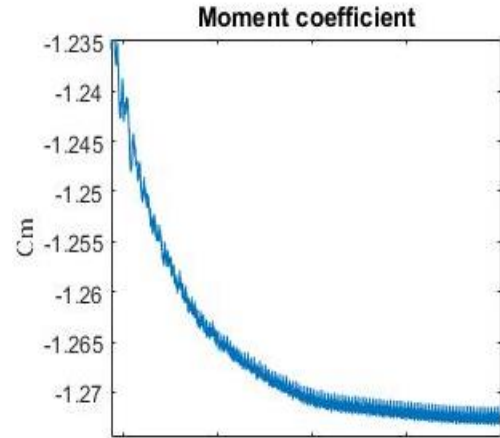


Figure 3.7. Moment coefficient convergence history

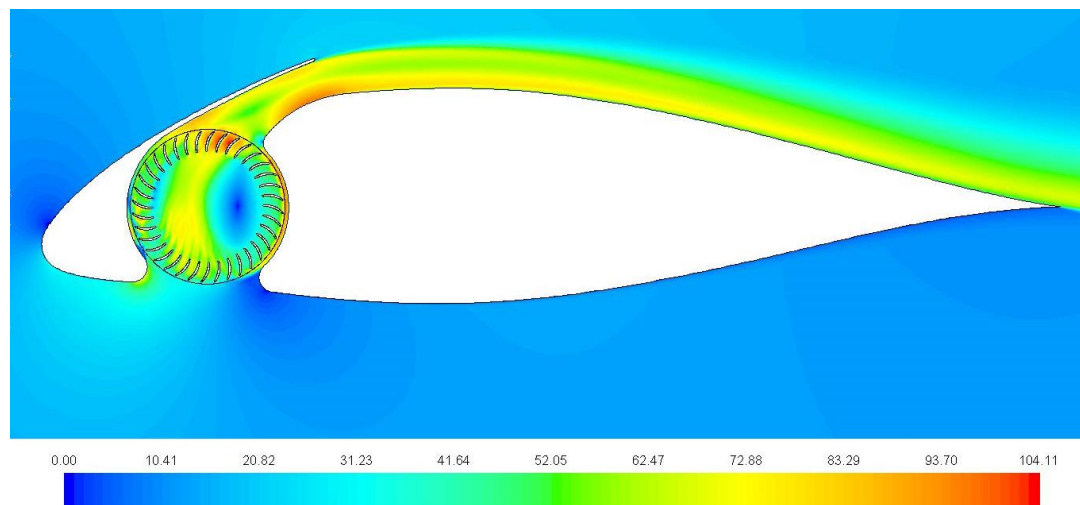


Figure 3.8. Velocity distribution on the airfoil with the Fan in m/s

Results show increase in the lift coefficient with angular velocity, but also increase in the required power per unit span to operate the fan. This fact puts a constraint on the fan sizing due to the extra power required for the engine and the weight penalty associated with it. The span sensitivity analysis of the CFF airfoil at different fan RPM is shown in

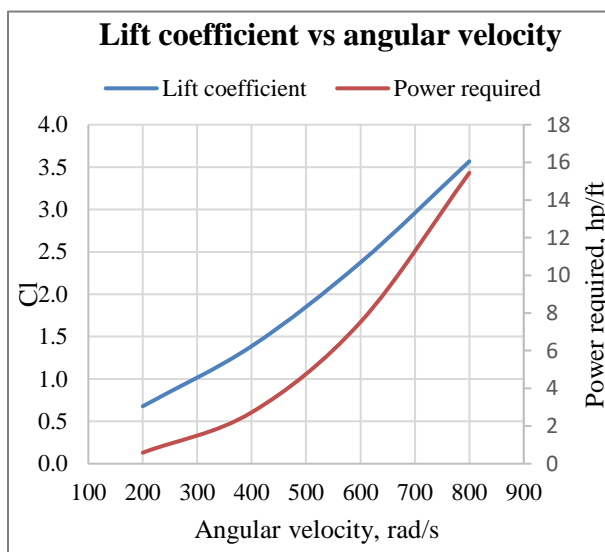


Figure 3.9. Convergence history of the

Figure 3.10 and demonstrates a linear increase in the required power with the span. It should be noted that an excessively high fan RPM would entail an unreasonable power requirement for the aircraft engines. Thus, the fan angular value of 400 rad/s with the fan embedded over 50% span of the wing was chosen as a good compromise between power required and aerodynamic benefits gained with the fan. Additional studies were performed

to investigate effects of the free-stream velocity on the airfoil aerodynamics at different angles of attack. Free-stream velocities of 5m/s, 15 m/s, and 25 m/s were used to determine the aerodynamic performance of the airfoil with the embedded fan. To maximize the aerodynamic performance of the airfoil, the Fowler flap was used with the CFF airfoil. The maximum flap deflection of 30 degrees ensured no flow separation on the flap.

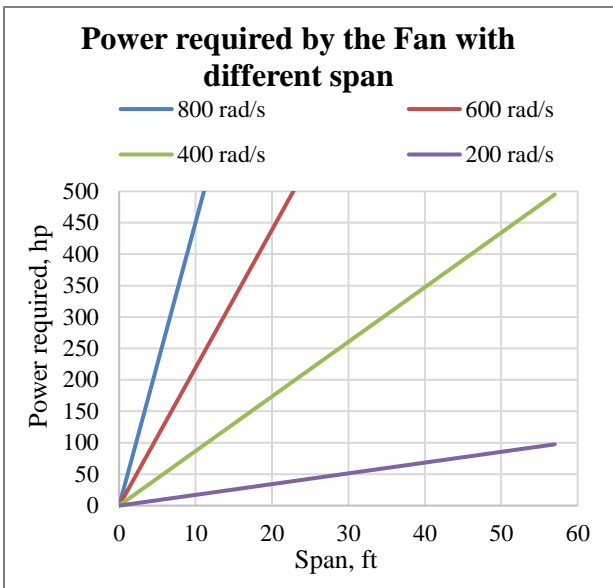


Figure 3.10. Convergence history of the CFF airfoil CFD solution

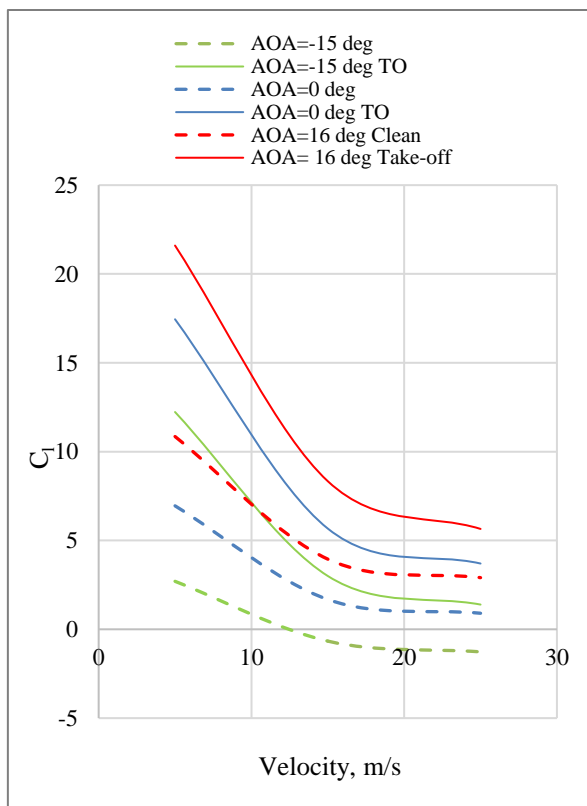


Figure 3.12. Velocity effect on lift coefficient

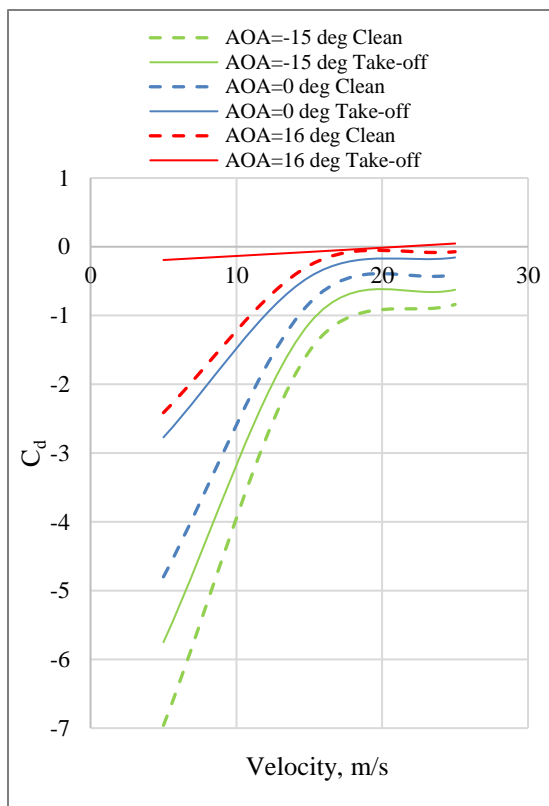


Figure 3.11. Velocity effect on drag coefficient

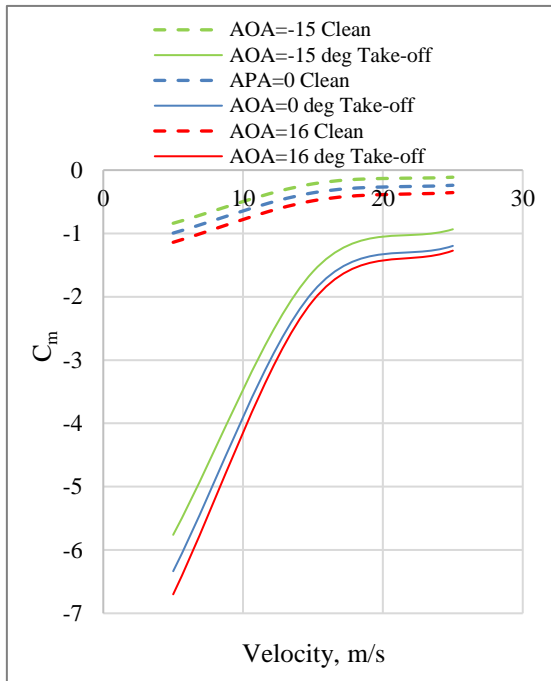


Figure 3.13. Velocity effect on moment coefficient

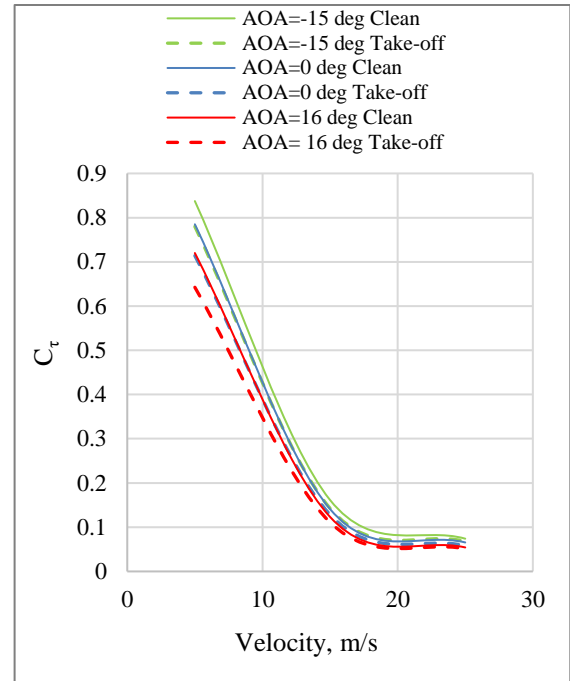


Figure 3.14. Velocity effect on torque coefficient

The results presented in Figures 3.11-3.14 demonstrate a notably high lift, moment, and power coefficients particularly at low speeds, with their substantial reduction at higher speeds with approaching the asymptotic values. Drag for the Fan-embedded airfoil is negative, so the system produces thrust; however, thrust diminishes with airspeed. Such trends is observed both for the clean and the flapped configurations.

Figure 3.15 shows the velocity distribution on the airfoil with the Fowler flap. Results for the same range of airspeeds and angles of attack were obtained and compared to the baseline conventional high-lift devices and the CFF airfoil without the fan. Figures 3.16 and 3.17 show comparison between the conventional high-lift devices, the fan without the Fowler flap and the fan with the flap.

From the Figure 3.16, the lift coefficient is increased due to the Fowler flap. With the increase of lift, moment coefficient decreases.

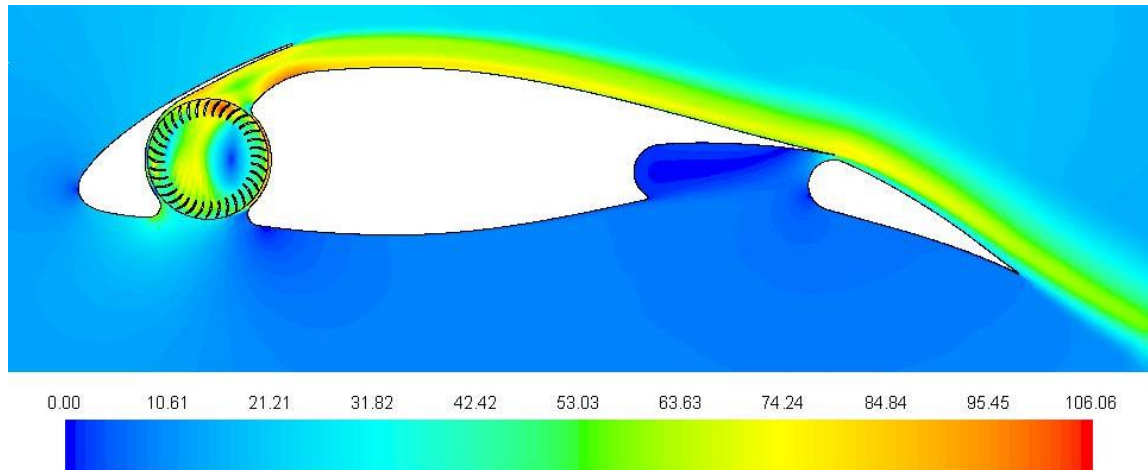


Figure 3.15. Velocity distribution on the airfoil with the Fan and the Fowler Flap in m/s

On the other hand, the magnitude of such decrease is very substantial to cause stability and control concerns during take-off and climb. Drag coefficient also increases due to the presence of the flap, while the torque coefficient remains relatively constant compared to the clean airfoil. Figure 3.17 shows comparison of airfoils with and without the fan and different flap configurations. In addition, comparison with Phan's results for clean NACA 63418 airfoil and with a simple flap deflected by 35 degrees is presented for validation. From the figures, conventional high-lift devices outperform the CFF airfoil without the flap. The only option for the clean airfoil with the fan to outperform the conventional high-lift devices is to increase the fan RPM, which will require extra engine power and weight increase and thus will affect the airplane en-route performance. The Fowler flap installed on the CFF airfoil significantly increases its lift coefficient compared to conventional high-lift devices, but also substantially increases the pitch-down moment. Comparison with Phan results show similar trend of lift and moment behavior for airfoils with the CFF, although different airfoils and high-lift devices were used.

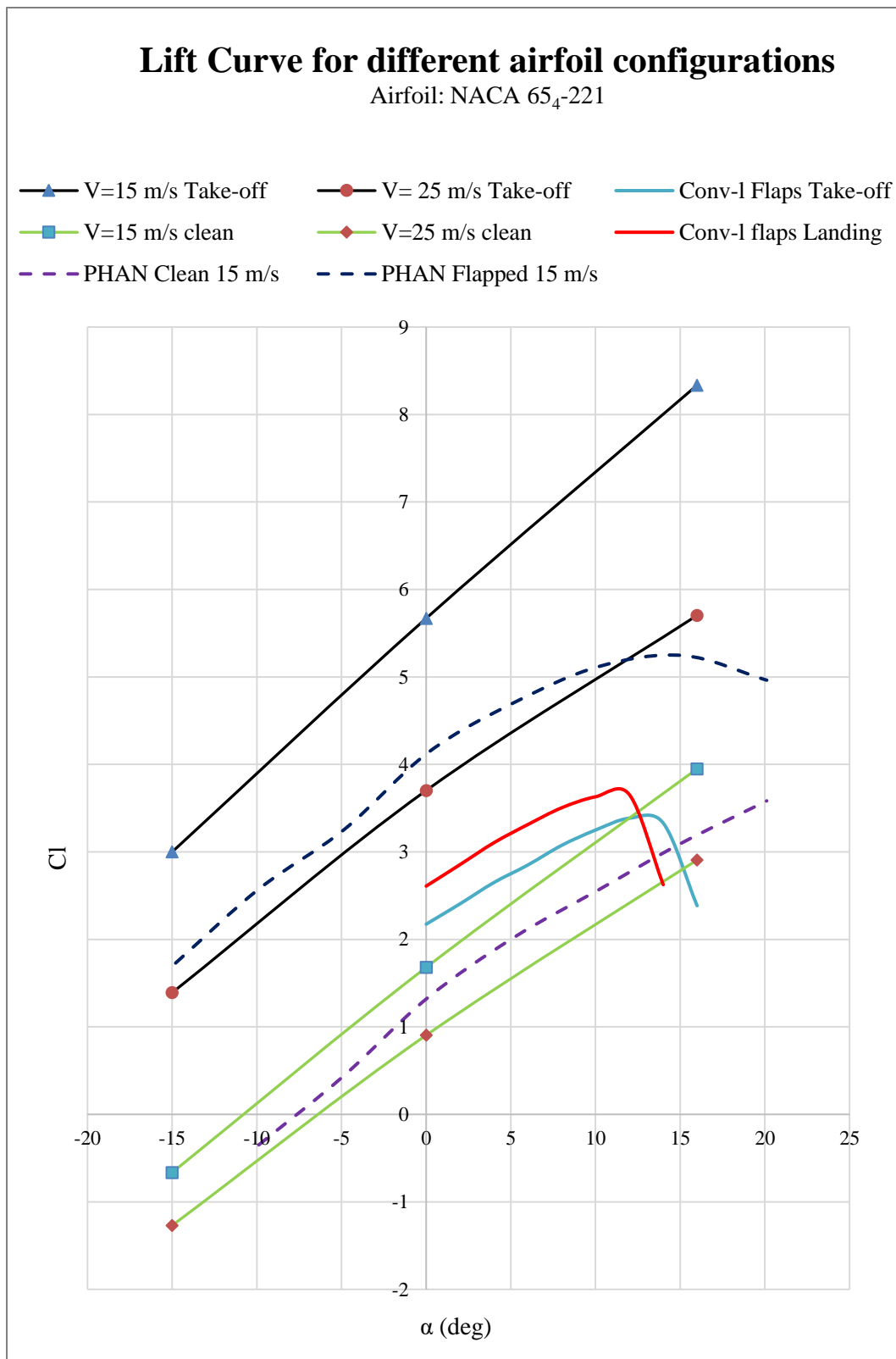


Figure 3.16. Lift curves for different airfoil configurations

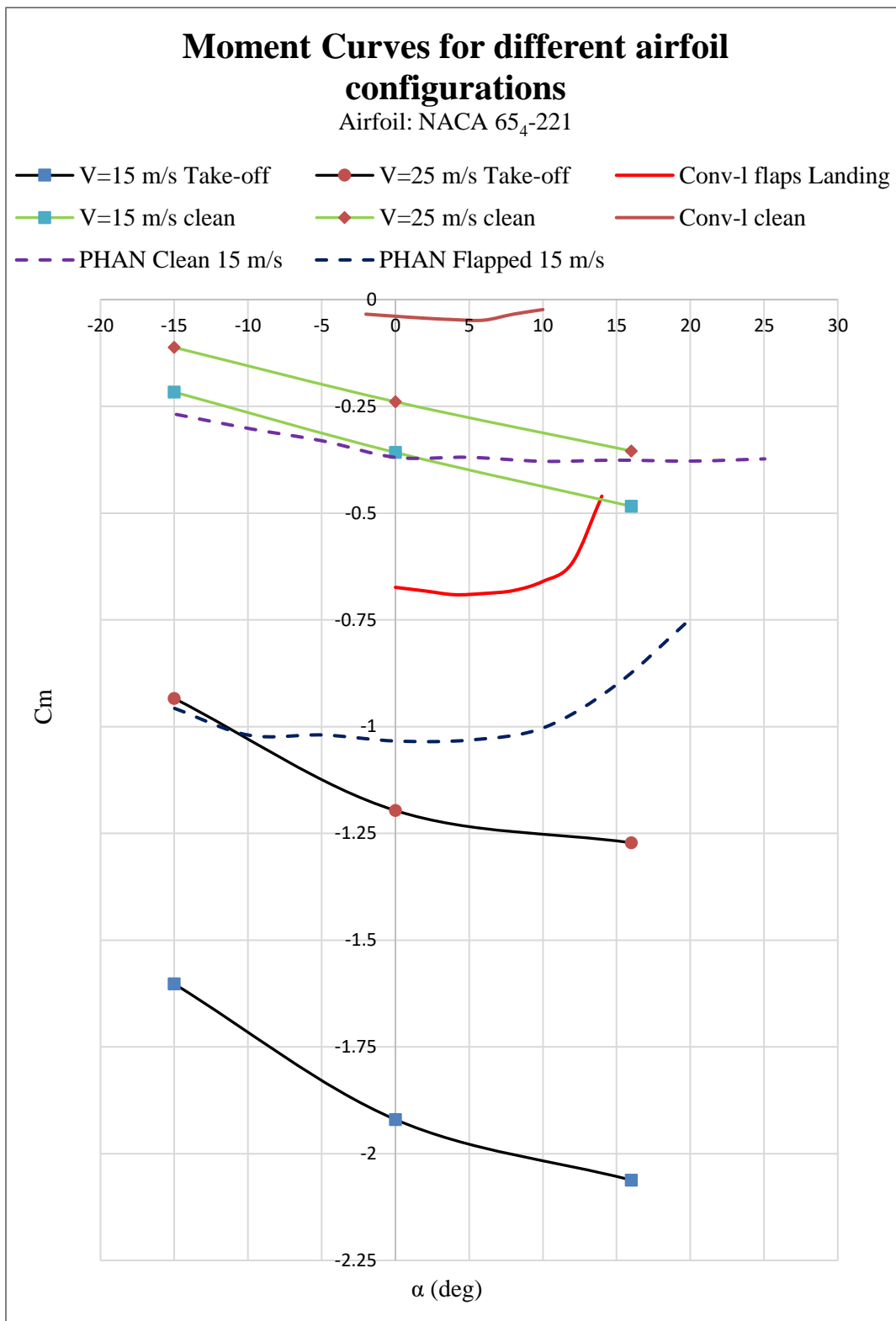


Figure 3.17. Moment coefficients for different airfoil configurations

4. Airplane Modifications and performance comparison

After obtaining aerodynamic coefficients for airfoils with the embedded fan, the Baseline aircraft configuration was modified to achieve required performance cruise characteristics. To transform CFD data for the airfoil to the wing, two steps are required. First, as long as the aircraft has a larger chord length comparing to the one used for CFD simulations, a new angular velocity and the required power must be obtained to transform the fan performance to a different airfoil chord length and preserve the fan flow physics. Consequently, flow coefficients for the tested airfoil and the design one must be same, so

$$\varphi = \frac{V_{\infty}}{\omega D} \Big|_{CFD} = \frac{V_{\infty}}{\omega D} \Big|_{Aircraft} \quad (4)$$

Equation (4) can be solved for the new angular velocity required for the modified aircraft and is equal to 312 rad/s. Then, the new power required for the CFF can be obtained using equations (2) and (3).

Based on the fan span trade study, extra 446 hp are required for the take-off and climb until the climb speed is reached. Additional power can be consumed from the engine, so the maximum power that can be used for thrust is 446 hp less than for the Baseline aircraft. Another solution is to include an additional APU which will be responsible only for the fan operation during the take-off and landing. Three cases, with Baseline engines (Model 1), with new engines having additional 446 hp (Model 2), and the Baseline engines with the additional APU (Model 3) were studied, and the airplane performance was compared to the Baseline model. PT6A-45A with 1020 hp was used for the Model 2 as the closest engine terms of the power required to compensate the fan power consumption, thus 797 hp is

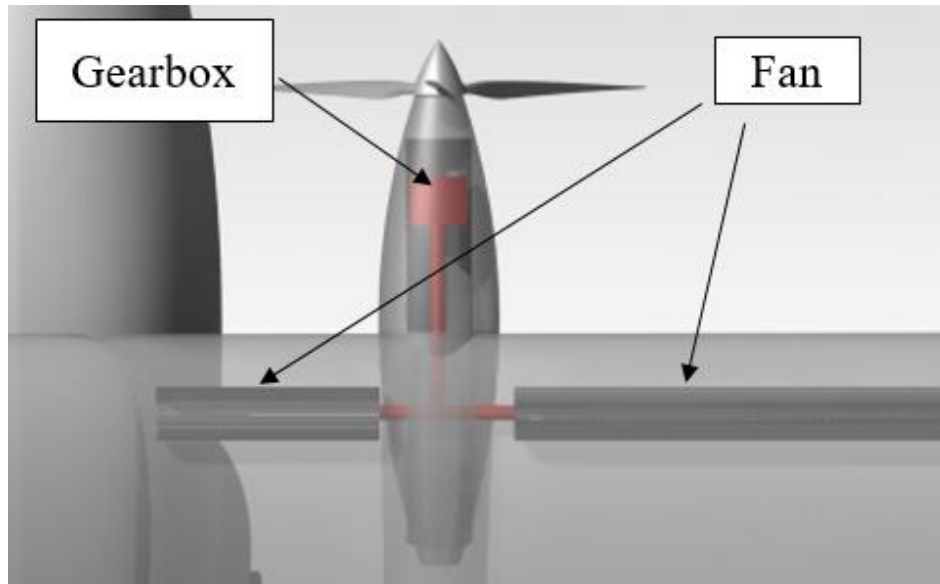


Figure 4.1. Gearbox and shaft layout for models 1 and 2

available for the take-off. Additional gearboxes for each engine adjust the fan angular in velocity and translate power from the engine to the CFF during the take-off and landing. For other mission segments, the CFF is switched-off, so all engine power is delivered to the propeller. Weight of the gearboxes was estimated using Torenbeek and is equal to 216 lb. An estimation of extra 242 lb for the fan system based on the fan blade volume and Magnesium AZ31B-H24 (Niu, 1988) material selection due to its weight and strength combination was made.

Table 4.1. EMRAX engines specifications

	EMRAX 228	EMRAX 348
Casting Diameter (mm)	228	348
Axial length (mm)	86	107
Continuous power (kW)	55	150
Dry mass (kg)	12.3	40

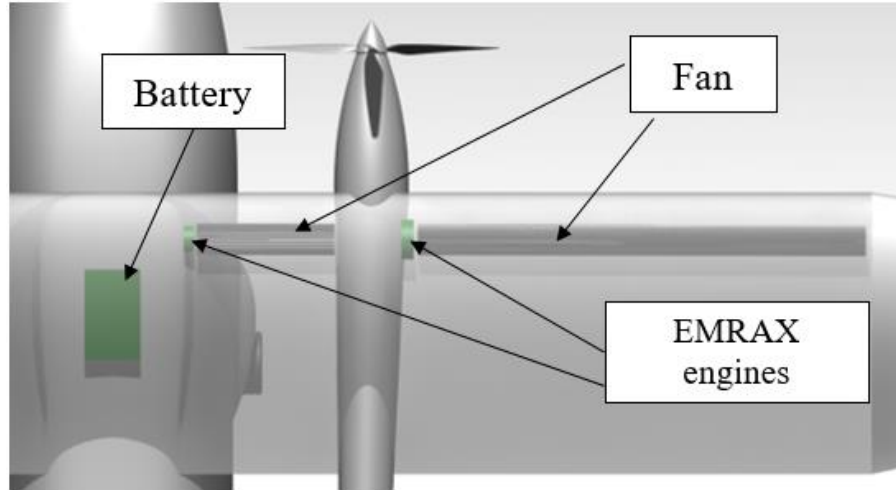


Figure 4.2. Model 3 Electrical system layout

The layout of the system for Models 1 and 2 is presented in Figure 4.1. For the APU, four EMRAX electric engines were used. Two EMRAX 228 were used for the inboard fan sections, while two EMRAX 348 were used for the outboard portions. Table 4.1 shows the EMRAX engine specifications. Total APU weight addition was 231 lb. Operation of the CFF was assumed to be 3 minutes for both the take-off and landing, and a Li-Po battery with 220 Wh/kg specific energy was assumed. Assuming extra 15% of battery weight required for wires and the battery mount, overall battery weight was 190 lb. Figure 4.2 shows the layout of the electric APU system. To equally compare the Baseline model and the ones with the embedded CFF, the maximum take-off weight was constant and equal to the Baseline weight. To adjust the weights, the payload weight for modified models was reduced. Airplane gross weight is calculated by

$$W_0 = \frac{W_{crew} + W_{payload} + W_{misc}}{1 - \frac{W_f}{W_0} - \frac{W_e}{W_0}} \quad (4)$$

where W_{misc} is additional weight due to the fan, the APU, the batteries, or other additional components of the airplane.

Additional weight contribution to the modified models was forced by static stability and trim requirements at low speed during the take-off and landing. The horizontal tail span of the modified models was increased to 16 ft and the chord was increased to 6.25 ft, as shown in Table 4.2.

Table 4.2. Geometric configuration changes for the CFF aircraft

		Baseline		CFF aircraft
	Wing	Horizontal Tail	Vertical Tail	Horizontal Tail
Span (ft)	66	15.00	9	16.00
AR	10.00	3.50	4.20	2.56
Root Chord (ft)	7.20	5.50	5.50	6.25
Taper Ratio	0.50	1.00	0.50	1.00
Incidence (deg)	3.00	-1.00	0.00	-2.00
LE Sweep (deg)	0.00	0.00	20.00	0.00
Volume coefficient		0.67	0.067	0.84

Table 4.3 summarizes weights of the Baseline and the modified airplane models. From the Table, introduction of the CFF and additional modifications of the Baseline configuration increase empty weight by 3.9%, 7.6%, and 5.9% and decrease maximum payload weight by 9.0%, 17.6%, and 13.6% for Models 1, 2, and 3 respectively. Model 3 show the largest savings in payload compared to other competitors. Performance characteristics of the modified models were compared to the baseline model and each other to determine the best airplane configuration. At the preliminary stage, the wing was assumed to have no adverse effect of the bottom gap required for the CFF operation.

Table 4.3. Weights comparison

	Baseline	Model 1	Model 2	Model 3
Maximum Take-off Weight (lb)	16187	16187	16187	16187
Empty Weight (lb)	9684	10064	10424	10254
Maximum Payload Weight (lb)	4200	3820	3460	3630

The take-off was estimated using dynamic analysis presented in Gudmundsson. Three-dimensional lift and drag for the fan-embedded wing were estimated using Wing Partition Method (Gumundsson, 2013), where two-dimensional aerodynamic properties from Figure 3.11 were used. Induced drag was obtained using the modified drag model shown in equation (1). Table 4.4 demonstrates take-off distances for all models.

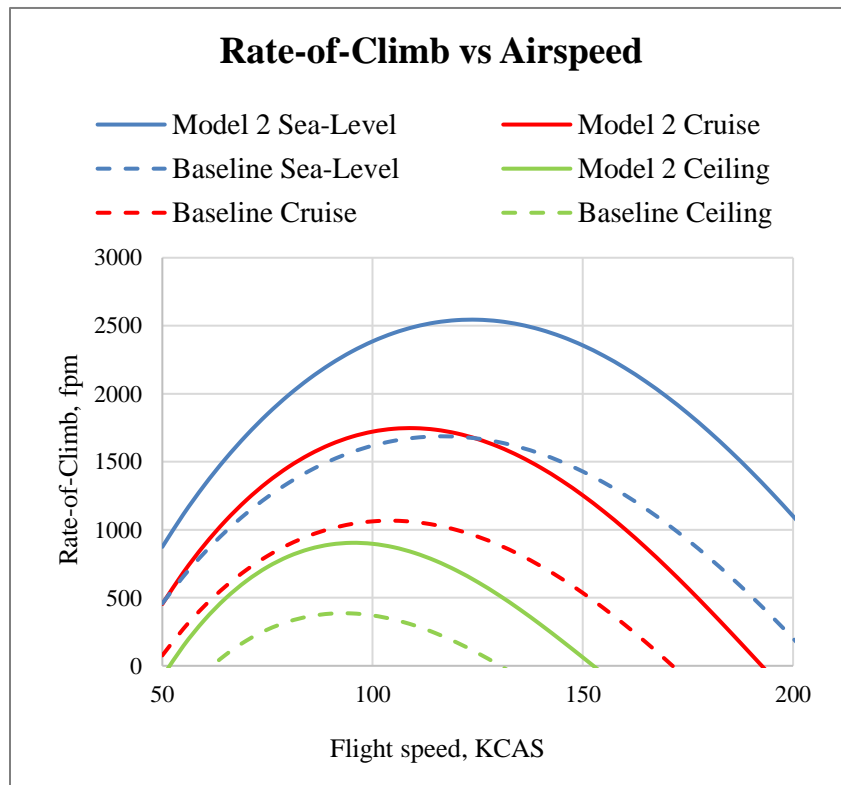
Results show that Model 2 has superior take-off characteristics comparing to the electric variant. However, the PT6A-45A had 47 hp more for the take-off because it was the closest engine in terms of the required power. The Model 3 also shows improvement in the take-off distance using same engines as the Baseline model, but the take-off distance was longer comparing to the Model 2. The Model 1 does not show improvements in take-off distance due to power losses to operate the CFF.

Climb performance of the Model 2 increases due to more powerful engines installed in the airplane. Maximum rate-of-climb is shown in Figure 4.3 and is equal to 2544 fpm. From Figure 4.4, the range of the modified models is reduced compared to the Baseline by 60 nmi.

Table 4.4. Take-off performance comparison

	Baseline	Model 1	Model 2	Model 3
Take-off distance (ft)	1912	2106	1493	1570
% difference	0	10.1	-21.9	-17.9

As for the maximum speed, Model 2 has maximum cruise speed of 227 KTAS at the cruise altitude while other models have the same flight envelope compared to the Baseline model, as shown in Figure 4.5. Based on the presented trade studies, both Models 2 and 3 have a potential to take-off from shorter fields compared to the Baseline model. However, the reduction in the take-off distance decreases the maximum possible payload with the same order of magnitude comparing to the Baseline airplane, so the trade between reduction in the take-off distance and the maximum payload may be problematic.

**Figure 4.3.** Climb performance comparison

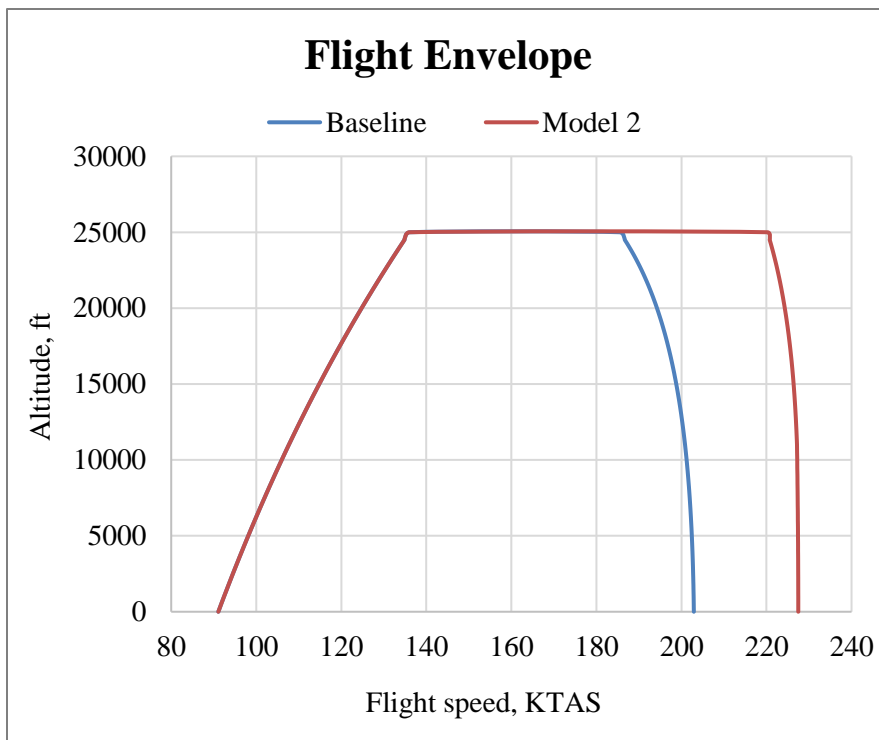


Figure 4.5. Payload-Range diagrams comparison

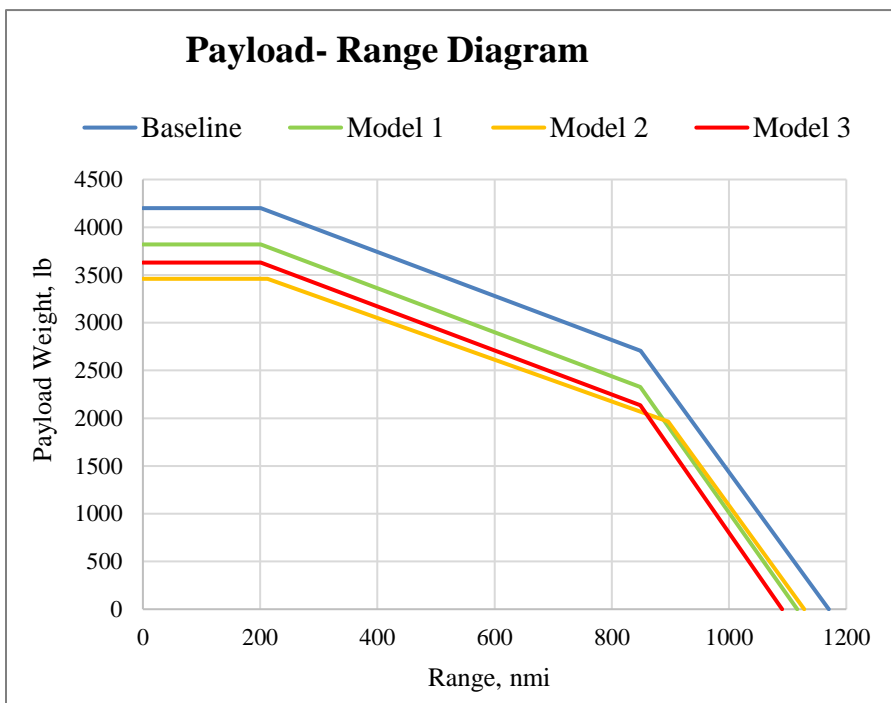


Figure 4.4. Flight envelope comparison

5. CFF aircraft scaling analysis

Previous analysis demonstrated that the effect of the CFF is not as significant as was expected. In addition, the payload weight penalty is of the same order as the gain in the take-off efficiency. The question is how the CFF affects aircraft of different categories and where the potential of the CFF can be best executed. To estimate the behavior of the CFF for different aircraft and quantify the performance during the take-off, a scaling analysis was performed

For the scaling analysis, the Model 3 configuration was used for all airplanes, so each aircraft had a battery that powered the set of fans for the total time of 3 minutes. Knowing the geometric and performance characteristics of the aircraft, the aircraft were modified to have an imaginary CFF embedded with the fan span of 50%. In addition, it was assumed that each modified wing would use the NACA 654-221 airfoil applied for the previous study. The fan then would be scaled in size and the RPM would be modified such that the flow coefficient for the modified wing would be consistent with the modified airplane studied above. Based on the modifications, a new take-off run and the weight change would be calculated using the methods used for the modified model calculations as for the airplane studied before. A set of existing GA aircraft lighter than 16000 lb were chosen. The take-off performance of the modified models with the embedded CFF and the baseline take-off distances were compared to estimate the gain in take-off efficiency.

In addition, the weight penalty was also compared between the baseline models and the modified ones. It is important to note that the modified airplanes featured a semi-tapered wing with the equivalent wing area as in the example case of the modified aircraft. Generally, that affects the overall performance of the airplane, so a more detailed analysis

of each aircraft is required to estimate the take-off performance for the original wing configuration more accurately. The present study is a simplified estimation of potential benefits of the CFF for given GA aircraft. Results demonstrated in Figures 5.1 and 5.2 show the percent difference between the baseline take-off distance and the CFF take-off distance for a given airplane. Figure 5.1 shows the take-off field length with the 50 ft obstacle as a function of the MTOW and Figure 5.2 presents the ground roll distance. From Figures 5.1 and 5.2, the CFF has more benefit in take-off distance improvement with the lighter aircraft reaching almost 40% for the 2500 lb airplanes like Cessna 172. With the

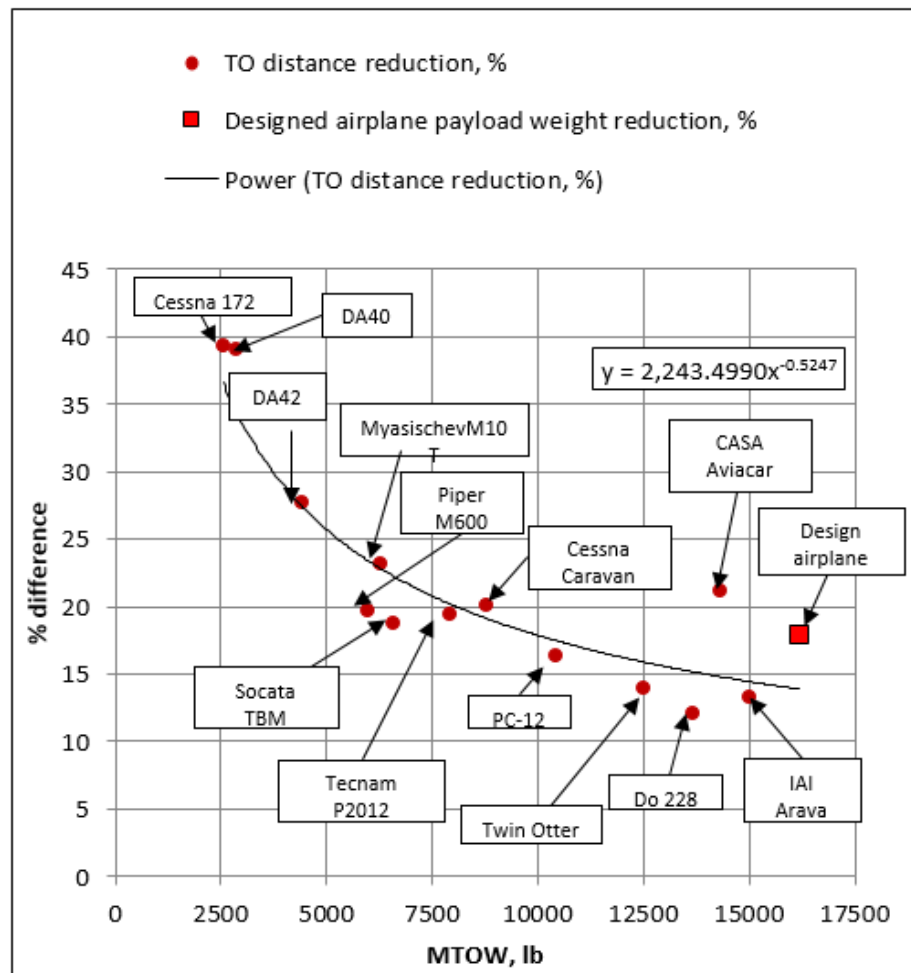


Figure 5.1. Take-off field length scaling analysis

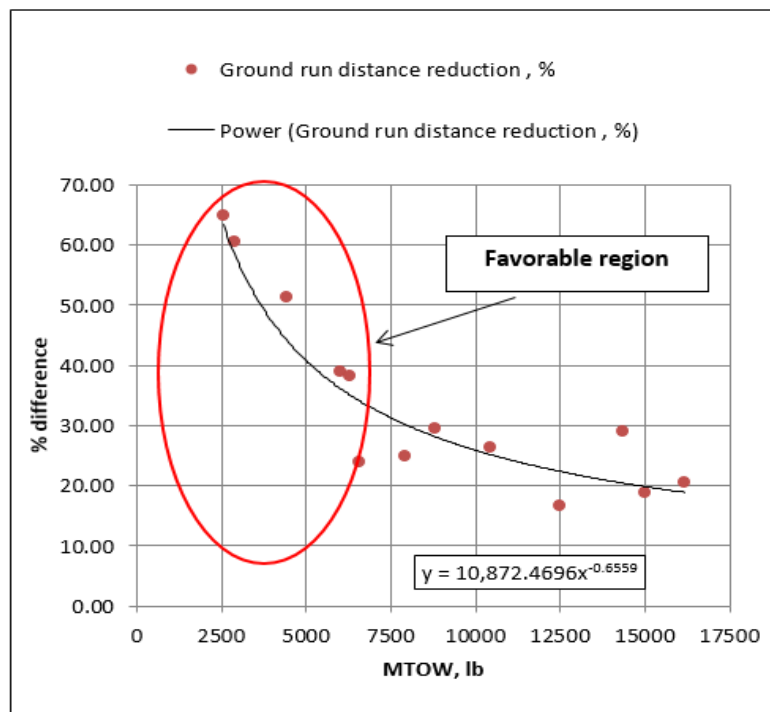


Figure 5.2. Ground roll scaling analysis

increase of the MTOW, the effect of the CFF reduces exponentially demonstrating a significant reduction in the ground roll distance. The ground run results shown in Figure 5.3. The aircraft of 2500 lb can reduce the round roll by 65% compared to the baseline ground roll. With the increase of the MTOW, the benefit of the CFF reduces exponentially reaching 20% for a 16000 lb airplane.

As for the payload weight reduction due to the CFF presence, Figure 5.3 shows a similar trend where up to 25% of the payload weight can be lost for the 2500 lb airplanes which may be equivalent to one passenger seat. The weight penalty also exponentially decreases with the MTOW reaching the values of 12% for 16000 lb airplanes.

A similar trend can be observed if the aircraft are compared as a function of wing loading, as shown in Figure 5.4. From the figure, take-off benefits and payload weight penalties show a similar trend like in previous comparisons, so lower wing loadings are more favorable for take-off distance reduction.

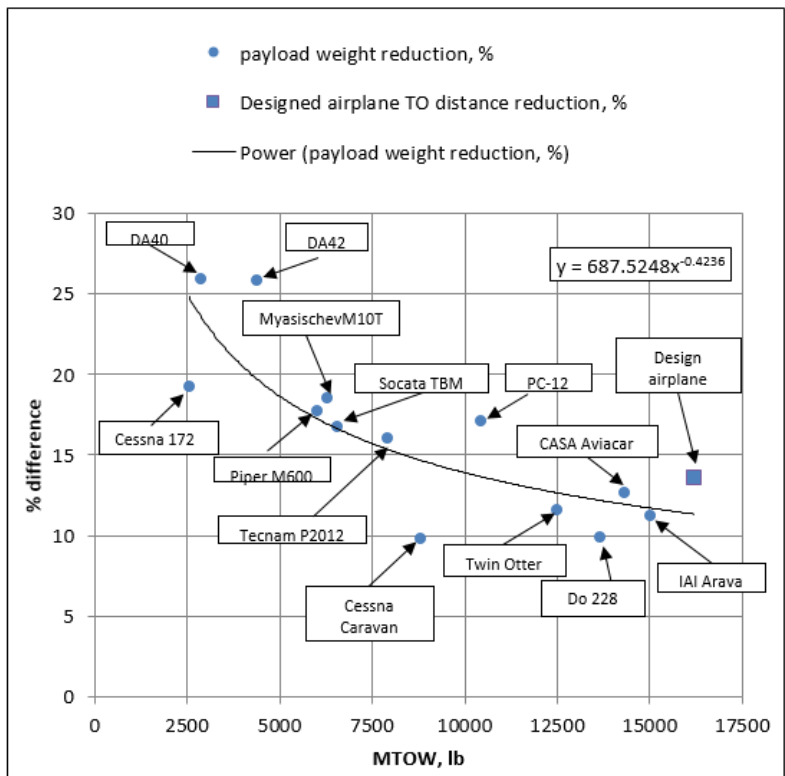


Figure 5.3. Payload weight scaling analysis

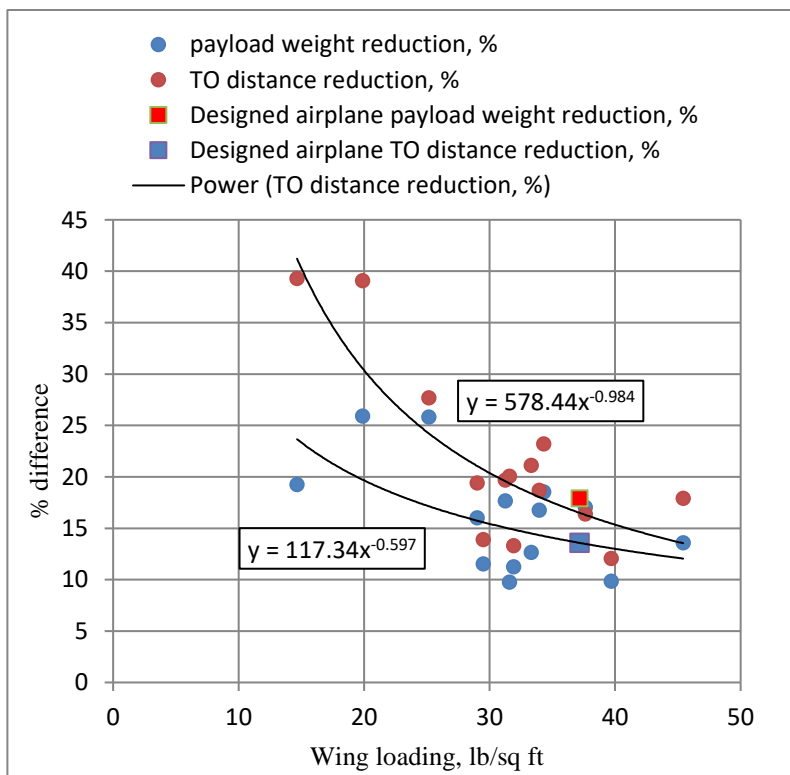


Figure 5.4. Payload and take-off distance scaling as a function of wing loading

To compare the effects of the CFF on the take-off istance and the payload weight, a cost function was introduced. The cost function is defined as

$$cost = \frac{f(MTOW)}{g(MTOW)} \quad (4)$$

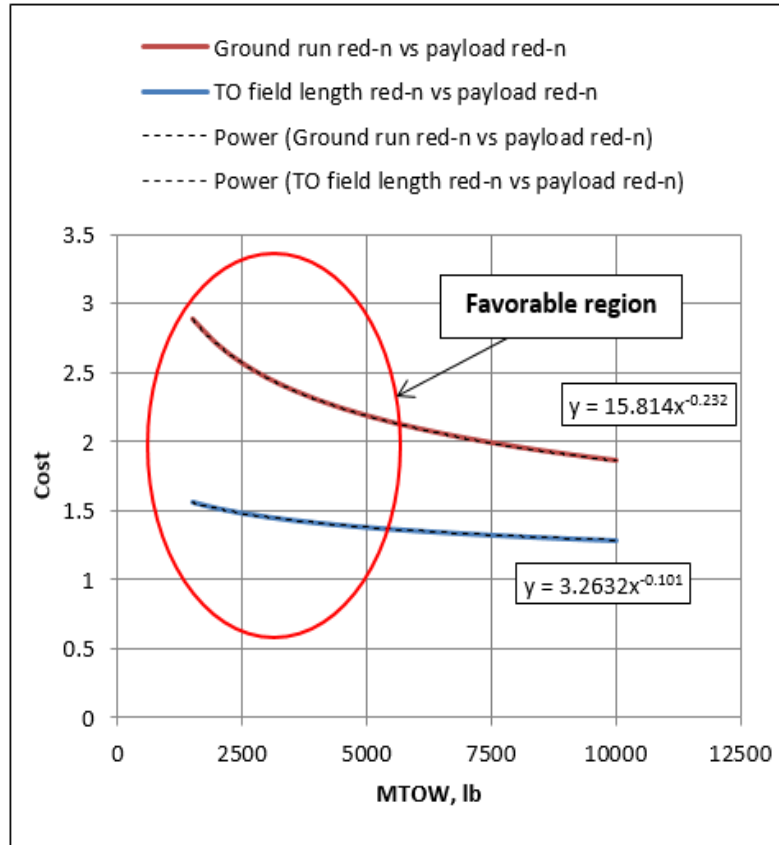


Figure 5.5. Cost function analysis results

where $f(MTOW)$ represents the curve-fitted function of the take-off or a ground roll distance from Figures 5.1 and 5.2 and $g(MTOW)$ represents the curve-fitted function of the payload weight penalty from the Figure 5.4. The cost analysis of the CFF effects is shown in Figure 5.5. From the results, the cost functions for both ground roll and the take-off field length have larger values for lighter airplanes and exponentially approach a constant with the gross weight increase.

From the results of the take-off and payload weight changes for specific MTOW, a favorable region lays in the range between 2500 lb and 7000lb where the benefit of the CFF significantly reduces the ground roll compared to heavier airplane configurations.

6. Performance of the CFF airfoil with the opened bottom gap

In section 4, the performance of the modified aircraft featuring the CFF was estimated assuming that the fan inlet is closed. However, the design of the system which closes the CFF inlet may be challenging and expensive, so an investigation of aerodynamic properties of the airfoil with an inoperative CFF at the cruise speed with the open inlet is done.

A computational domain of the CFF airfoil is shown in Figures 6.1 and 6.2. The slat is at the cruise configuration with the closed outlet and an open inlet of the fan. The mesh size was 163512 cells and the mesh is unstructured featuring a T-REX to resolve the boundary layer regions. Y^+ is

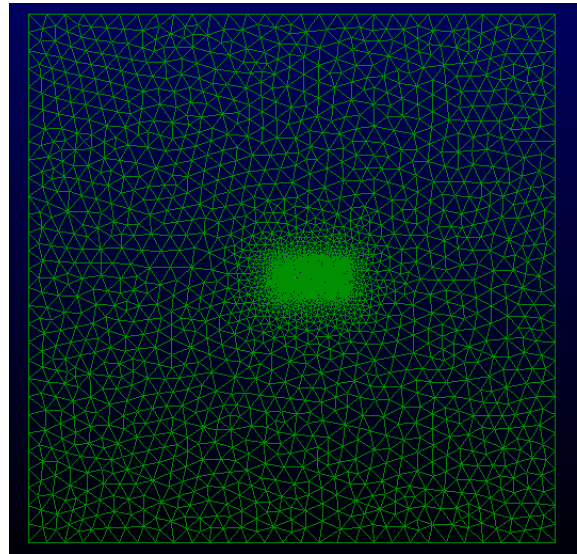


Figure 6.2. Airfoil CFD far-field mesh

equal to 1 to resolve the boundary layer behavior and far field is located 100 chord length away from the airfoil surface, which ensures the proper implementation of the far-field boundary condition. ANSYS Fluent Transient RANS with Transitional SST model was

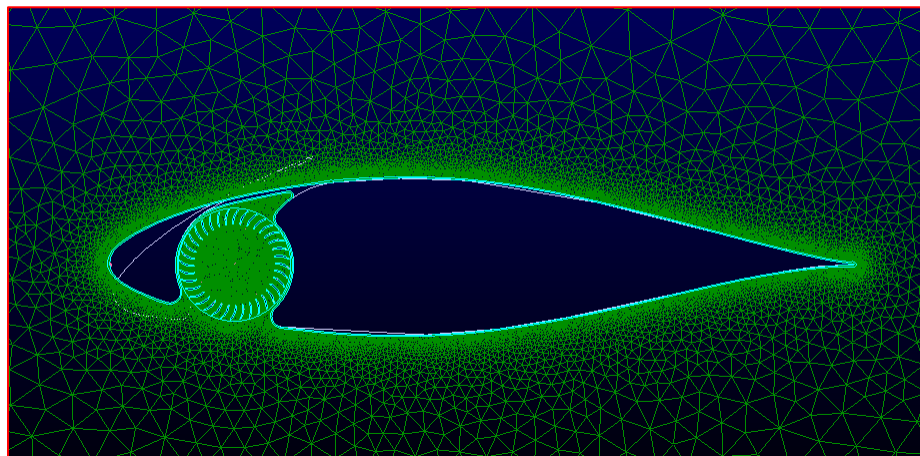


Figure 6.1. Airfoil CFD mesh

used to calculate the aerodynamic properties of the airfoil. The free-stream Mach number is equal to 0.28.

The pressure and velocity distributions comparison between the baseline airfoil and the CFF one are shown in Figures 6.3-6.6 for 0 and 14 deg angle-of-attack.

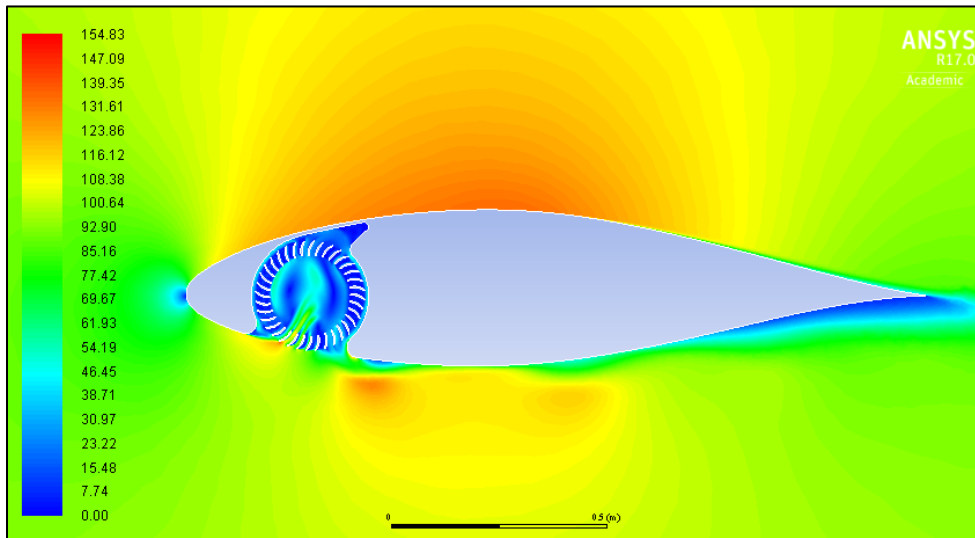


Figure 6.4. Velocity distribution at 0 deg AOA

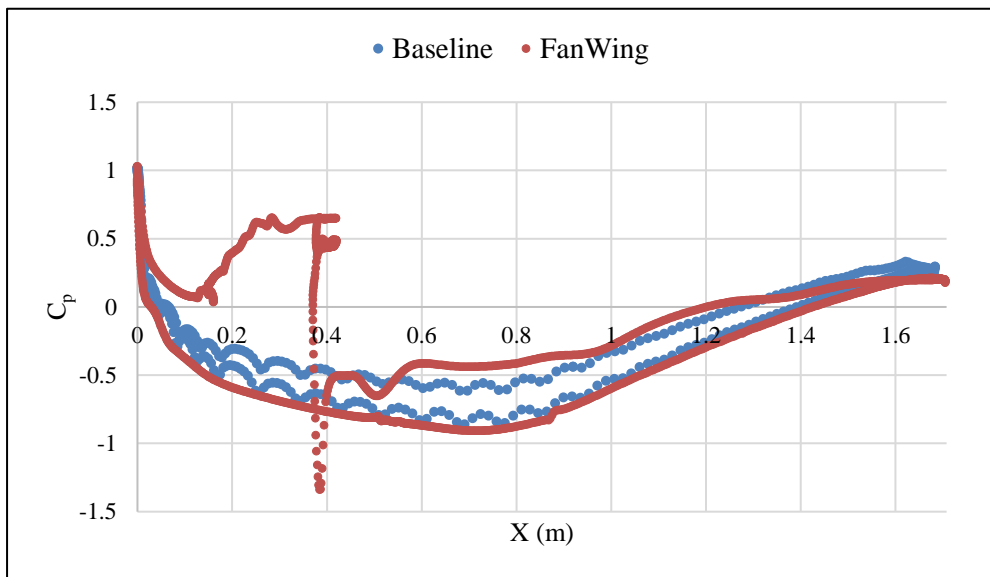


Figure 6.3. Pressure coefficient distribution for the CFF wing at 0 deg AOA

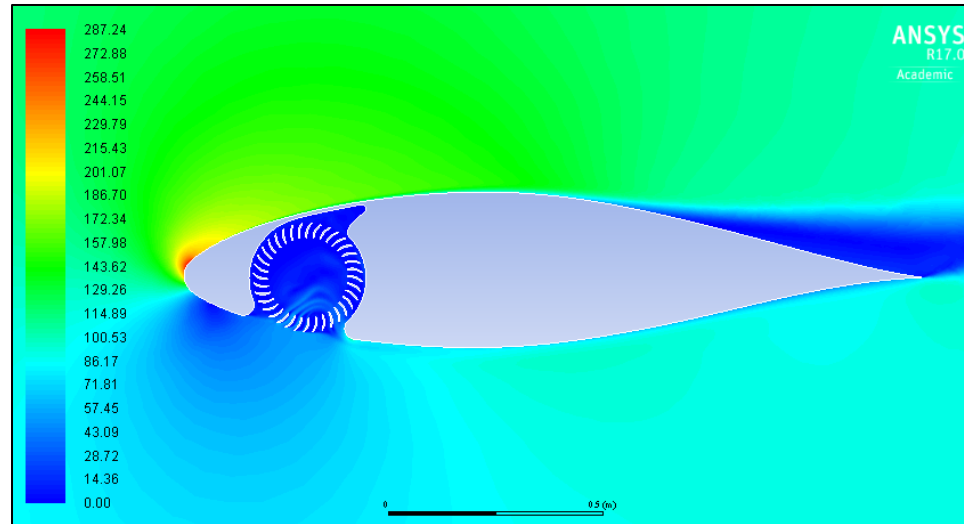


Figure 6.5. Velocity contour for the CFF wing at 14 deg AOA

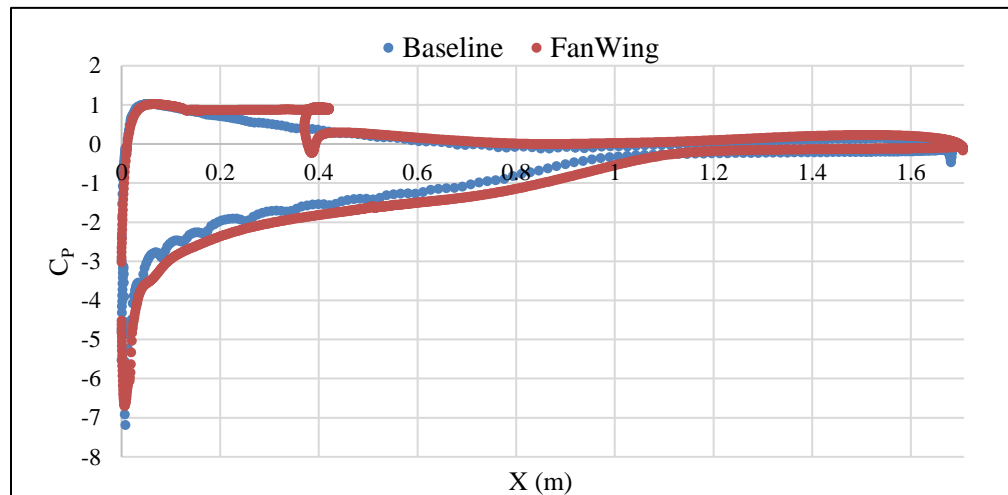


Figure 6.6. Pressure coefficient distribution for the CFF wing at 14 deg AOA

Results show an increase in pressure coefficient on the airfoil surface at the fan region for both angles of attack that caused increase in lift coefficient for the CFF airfoil at cruise conditions.

Figures 6.7 and 6.8 present the lift curve and the drag polar of the CFF airfoil and were compared to the experimental data from Abbot.

From the results, the lift curve of the CFF was shifted up due to the pressure increase at the fan region and the change of the airfoil effective camber. In addition, the presence of

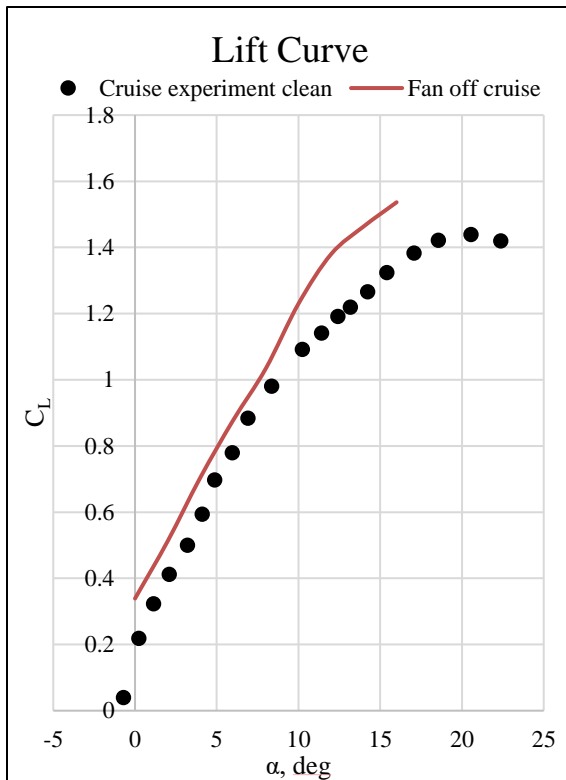


Figure 6.7. Lift curve for the CFF airfoil with a closed gap

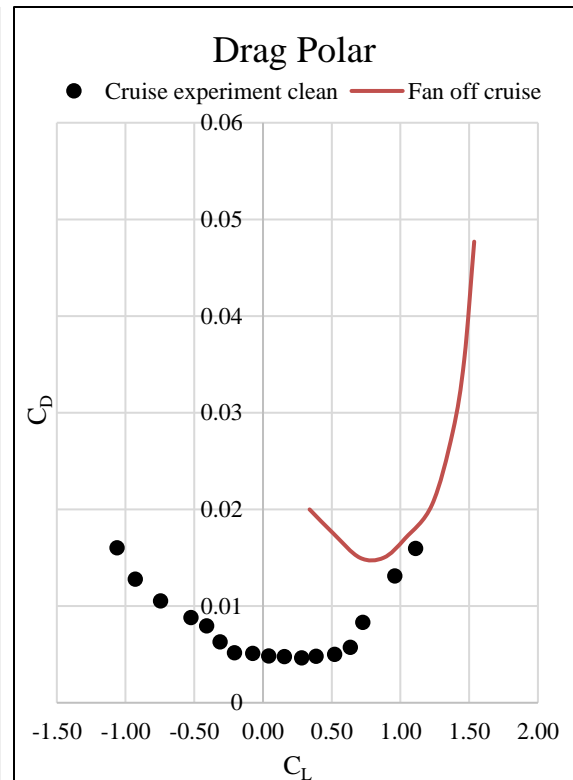


Figure 6.8. Drag polar for the CFF airfoil with a closed gap

the fan orifice increases the lift coefficient at higher AOA due to the effect described above. However, the orifice and the fan blades generate a lot of drag that shifts the drag polar to the polar up and increases the minimum drag coefficient by 3 times. In addition, the drag polar also shifted to the right due to the flow pattern inside the fan at different angles of attack. Velocity contours at several angles of attack are shown in Appendix A. at low AOA, the flow goes inside the fan at a relatively high speed generation a complex flow pattern and, consequently, drag. When the AOA increases, the flow speed inside the fan decreases mitigating the drag penalty due to the fan presence. As the fan AOA becomes large, a separation at the trailing edge provides additional drag component that increases the total airfoil drag.

To ensure accuracy of the solution, a mesh sensitivity study was performed. Table 6.1 shows results of the mesh sensitivity analysis. Base on the sensitivity analysis, the coarse and the fine meshes show similar results.

Table 6.1. Mesh sensitivity analysis

Mesh size	C_l	C_d
163512	0.331	0.02
205540	0.339	0.02

The aerodynamic results of the CFF airfoil with the opened gap show that the fan inlet must be sealed to ensure efficient cruise performance of the aircraft. However, the requirements of an additional mechanical system may increase the costs of the fan system and the complexity of design and manufacturing that are drawbacks of the technology

7. Fan failure cases aerodynamic sensitivity studies

A new technology should always be monitored to investigate potential failure modes, the effects of the failure cases on the aircraft performance and potential safety issues regarding the system failure. The CFF is a device which has moving parts and also a slat, so both mechanisms may fail during the take-off or landing. The purpose of this chapter is to investigate aerodynamic impacts of the wing-embedded CFF technology in case of the system failure and estimate risks regarding the failures.

In the present study, two failure variants were studied. The first case had the opened slat with a stopped fan as, for instance, the fan was 'jammed'. Figure 7.1 shows the CFD mesh of the airfoil. Here, the airfoil without the fan was considered as an example of the operational condition when the fan was working, but the flaps were retracted. That example models the climb stage of the take-off of the landing approach. A similar meshing approach was used as in previous experiments. Y^+ is equal to 1 to resolve the boundary layer. The mesh size is equal to 210000 cells. ANSYS Fluent was used to calculate the aerodynamic characteristics of the airfoil at the free-stream velocity of 20 m/s

Figures 7.2 and 7.3 show the lift and drag coefficients comparison between the baseline airfoil aerodynamic performance and the failed CFF airfoil. Lift demonstrates a downforce due to the flow pattern change due to the stopped fan. Increasing the angle-of-attack, the flow begins to go through the fan as shown in Figure B.3. The drag becomes large due to the stopped fan. In addition, the pattern of the drag polar does not follow the typical parabolic shape as in any classical airfoil due to the orifice and a complicated flow over the airfoil at different angles-of-attack.

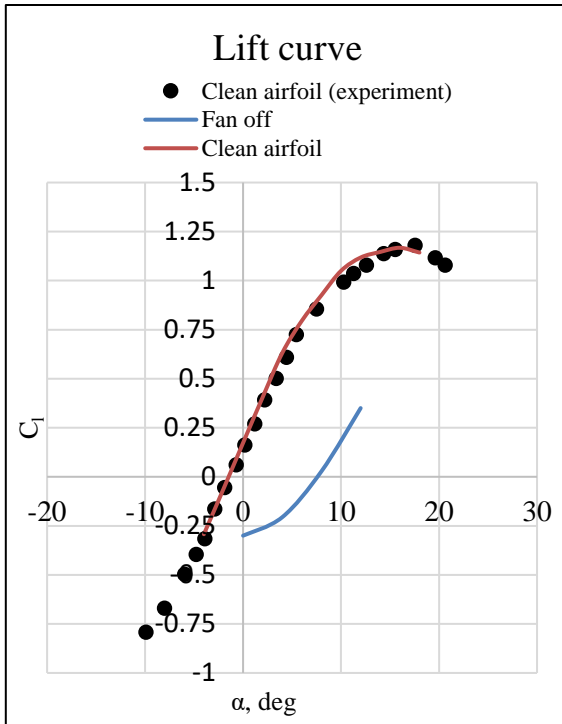


Figure 7.2. Lift curve for the CFF airfoil with a jammed airfoil

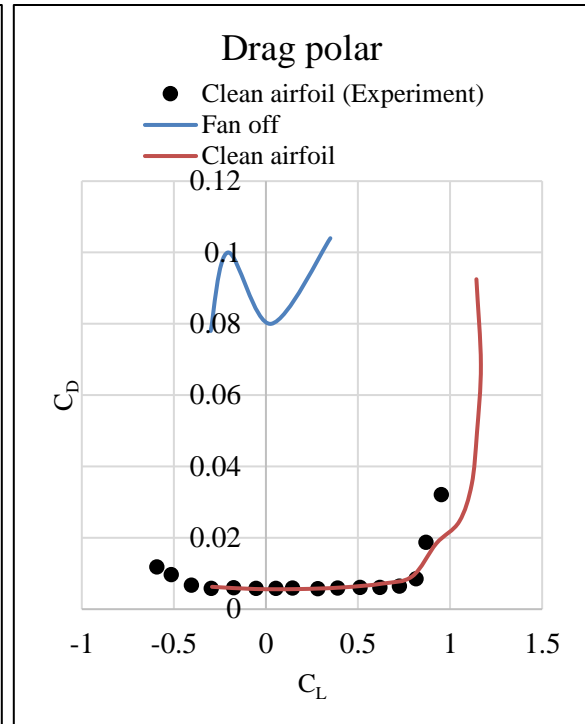


Figure 7.1. Drag polar for the CFF airfoil with a jammed fan

Consequently, the presented failure case is dangerous as long as the aircraft is operated at low altitudes during the take-off and landing mission segments: the aircraft will dive due to the downforce instead of generating lift. The system that returns the slat at the initial position must be designed to avoid the presented situation.

The second failure case deals with the slat deflection failure. The geometry and the computational domain are shown in Figure 7.3. There, the slat is not deflected, but the fan continues to rotate at the same RPM. As in the previous example, the flap is not deployed to simulate the climb region of the take-off and the approach during landing. The tested angle-of-attack is equal to 0 degrees and the free-stream velocity is equal to 20 m/s.

Aerodynamic results of the second failure case are shown in Table 7.1 where the baseline clean airfoil results are compared to the failed airfoil. In addition, the time-history of the transient CFD convergence is shown in Figures 7.4 and 7.5 and the velocity

streamlines are shown in Figure 7.6.

Result present positive average lift of the failed airfoil. However, as long as the flow on the pressure side is unsteady, lift experiences periodic lift with the amplitude of 0.25. Such unsteady behavior is undesired and creates substantial control difficulties for the pilot to operate the airplane. In addition, the airfoil drag is substantially increased due to spoiled flow on the pressure side.

Airfoil	C_l	C_d
Baseline	0.2	0.005
CFF airfoil	0.3	0.1

Table 7.1. Aerodynamic comparison of the failed airfoil case to the baseline

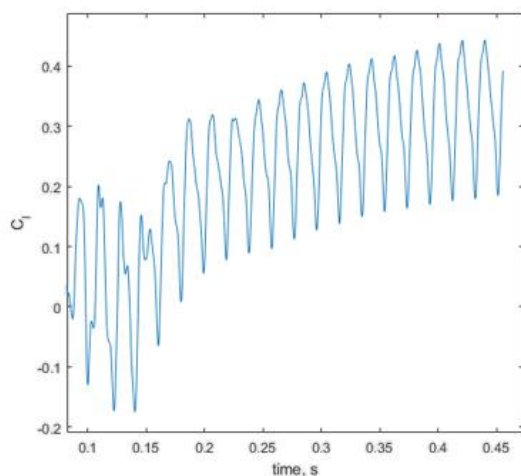


Figure 7.4. Convergence history of lift coefficient

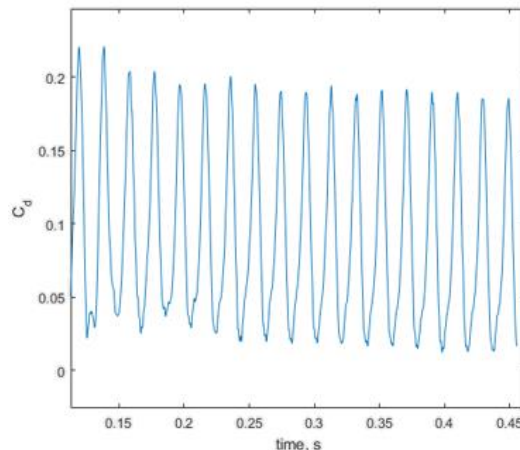


Figure 7.3. Convergence history of drag coefficient

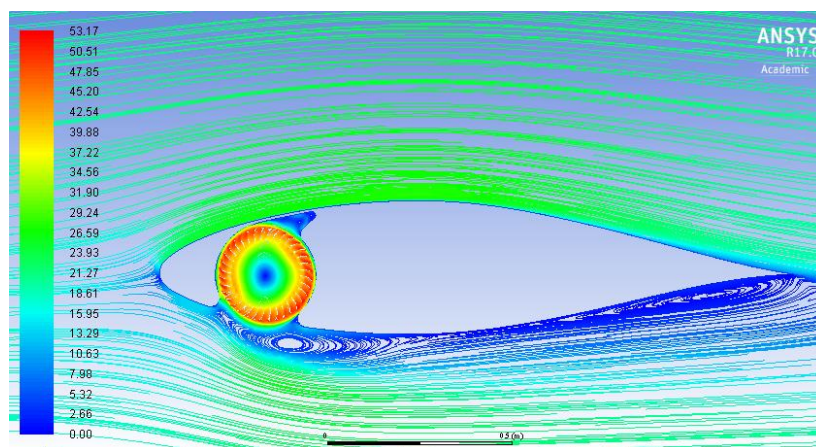


Figure 7.5. Velocity streamlines plot

8. Conclusion

In the current study, a preliminary feasibility analysis of the Cross-Flow Fan technology applied to a multi-purpose aircraft was performed. Two-dimensional clean and flapped CFF airfoil analyses showed improvement in the lift coefficient vs. the free-stream velocity. However, the fan benefits reduce with the airspeed, thus limiting the potential advantages of the CFF-based ESTOL technology. To estimate CFF performance on a multi-purpose General Aviation aircraft, a baseline concept comparable to benchmark airplanes without the fan, and three different airplane modifications with the fan, were designed. Two of the three models showed reduction in the take-off distance not exceeding 22%, but they suffered a maximum payload weight reduction of the same order of magnitude compared to the Baseline configuration for the same gross weight.

One of the models had a more powerful engine and gearbox to operate the engines and the fan during the take-off. In addition, due to the selection limitations, the employed PT6A-45A engine had more power available for the take-off, hence the take-off performance characteristics partially improved due to the engine choice. The cruise performance also improved in terms of the maximum flight speed and the rate-of-climb because of the more powerful engines.

Another model featured the same engines as the baseline configuration but also employed electric motors that drove the CFF. The maximum payload weight improved compared to the model with more powerful engines but revealed less benefits in the take-off distance.

Both models showed a good alternative to the baseline aircraft, but the payload/take-off trade may prove problematic in the modern commercial environment. Additional

challenges include maintenance requirements for the fan and its subsystems that may increase operational costs of the airplane. Safety challenges due to fan failure showed potential danger of the system failure and substantial difficulties operating the aircraft with unsteady lift provided by the failed system. Another potential problem is the acoustic radiation from the fan.

Scaling analysis demonstrated potential improvement of the CFF technology for lighter airplanes. Airplanes of the gross weight below 7000 lb may improve their ground roll by at least 40% while the take-off field length could be reduced by 25%. Although, the payload penalty remains, the benefit of the take-off distance is more significant than the payload loss.

It should be noted that the approaches used for the current study requires experimental validation to demonstrate a proof of the CFF concept.

9. Recommendations

Present work was a preliminary feasibility analysis of a specific type of airplanes in a particular category. The study can be extended to lighter aircraft where the CFF potential can be maximized.

In addition, specific questions in each subcategory of the CFF integration can be addressed. For example, structural analysis of the fan and more accurate weight estimations, acoustic effects of the wing-embedded CFF, and mechanical design of the system which closes the inlet door can be addressed to understand the complexity of the system better.

The feasibility analysis was made based on a semi-tapered wing configuration. A uniformly tapered wing has more aerodynamic benefits compared to the semi-tapered configuration, but it requires a more detailed 3D CFD analysis of the CFF-embedded wing because the flow coefficient varies along the wing span. That, in turn, will change the lift increment generate by the fan and power required by the APU. So three-dimensional effects of the CFF should be studied to better investigate its effect on tapered configurations.

Knowing all details described above, it is possible to finally quantify the benefits and drawbacks of the system, try to mitigate the disadvantages and find an appropriate market for the technology.

REFERENCES

- Abbot, Ira H.A., Von Doenhoff, Albert E. "Theory of Wing Sections Including a Summary of airfoil data", Dover Publications, New York, 1959
- ANSYS FLUENT 12.0 Users Guide, April, 2009.
- CFR FAR Part 23, Electronic code of federal regulations, May 25 2017, <https://www.ecfr.gov/cgi-bin/text-idx?rgn=div5&node=14:1.0.1.3.10>
- Chawla, K., "Optimization of Cross Flow Fan Housing for Airplane Wing Installation," M.S. Thesis, University of Texas at Arlington, Arlington, TX, 1984.
- EMRAX Innovative E- Motors. <http://emrax.com/>
- Goland, C., Mores, S., Steiner, H., Seitz, A., "Potential of the Cross-Flow Fan for powered-Lift Regional Aircraft Application", 9th AIAA Aviation Technology, Integration, and Operations Conference (ATIO), 21-23 September 2009, Hilton Head, South Carolina.
- Gossett, D. H., "Investigation of Cross Flow Fan Propulsion for a Lightweight VTOL Aircraft," M.S. Thesis, Naval Postgraduate School, Monterey, CA, Dec. 2000.
- Gudmundsson, S., "General Aviation Aircraft Design: Applied Methods and Procedures". Butterworth-Heinemann, Oxford, 2013.
- Hahn, A. S., "Vehicle Sketch Pad: A Parametric Geometry Modeler for Conceptual Aircraft Design," 48th AIAA Aerospace Sciences Meeting, American institute of Aeronautics and Astronautics, Orlando, FL, 2010, pp. 1 – 11, AIAA-2010-0657.
- Hahn, A. S., "Vehicle Sketch Pad Aircraft Modeling Strategies," 61st AIAA Aerospace Sciences Meeting, American Institute of Aeronautics and Astronautics, Grapevine, TX, 2013, pp. 1 – 9, AIAA-2013-0331.
- "IHS Jane's Aero Engines", Coulsdon Surrey, HIS Global Limited
- "IHS Jane's all world aircraft, Development and production", Coulsdon Surrey, HIS Global Limited
- Hahn, A. S., "Vehicle Sketch Pad Aircraft Modeling Strategies," 61st AIAA Aerospace Sciences Meeting, American Institute of Aeronautics and Astronautics, Grapevine, TX, 2013, pp. 1 – 9, AIAA-2013-0331.
- Kramer, B., Ansell, P., D'Urso, S., Ananda, G., Perry, A., "Design, Analysis, and Evaluation of a novel propulsive Wing Concept," Final Report, Rolling Hills Research Corporation, June 30th, 2016

- Kummer, J. D., Dang, T. Q, “High-Lift Propulsive Airfoil with Integrated Crossflow Fan,” AIAA Journal, Vol. 43, No. 4, 2006, pp. 1059-1068.
- Lin, C.-H., “A Wind Tunnel Investigation of the External Aerodynamics of an Airfoil with an Internal Cross Flow Fan,” M.S. Thesis, University of Texas at Arlington, Arlington, TX, 1986.
- Nelson. R, “Flight Stability and Automatic Control, 2nd edition”, WCB/McGraw Hill, Boston, Ma, 1998.
- Nicolai, L., “Fundamentals of Aircraft and Airship Design. Vol 1”, AIAA, Reston, VA, 2010.
- Nieh, T.-W., “The Propulsive Characteristics of a Cross Flow Fan Installed in an Airfoil,” M.S. Thesis, University of Texas at Arlington, Arlington, TX, 1988.
- C. Y. NIU, “Airframe Structural Design”, Conmilit Press, Hong Kong, 1988
- Pointwise Grid Generator, <http://www.pointwise.com/>
- Phan., N, H., “Leading Edge Embedded Fan Airfoil Concept – a new powered High Lift Technology”, PhD Dissertation, Syracuse University, Syracuse, NY, 2015
- Raymer, D., “Aircraft Design: A Conceptual Approach 5th edition”, AIAA, Washington, D.C., 2012.
- B. Stevens, “Aircraft control and Simulation, 2nd edition”, Wiley, Hoboken, NJ, 2003.,pp 284-286
- SURFACES, VLM Software package, Ver 2.0, Flight Level Engineering, <http://www.flightlevelengineering.com/surfaces>
- Torenbeek, E., “Synthesis of Subsonic Airplane Design, 2nd Edition”, Delft University Press, 1982.
- Young A.D., “Boundary Layers”. AIAA Education Series, 1989
- .

A. The CFF airfoil velocity contours at cruise

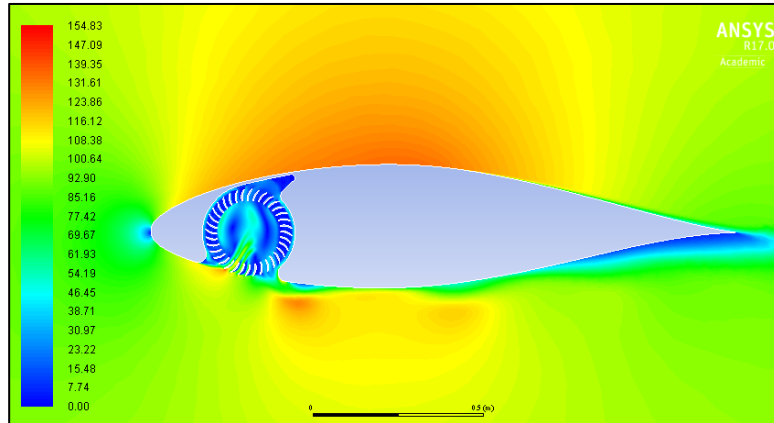


Figure A.1. Velocity contours at 0 deg AOA
($C_l=0.339$, $C_d=0.02$)

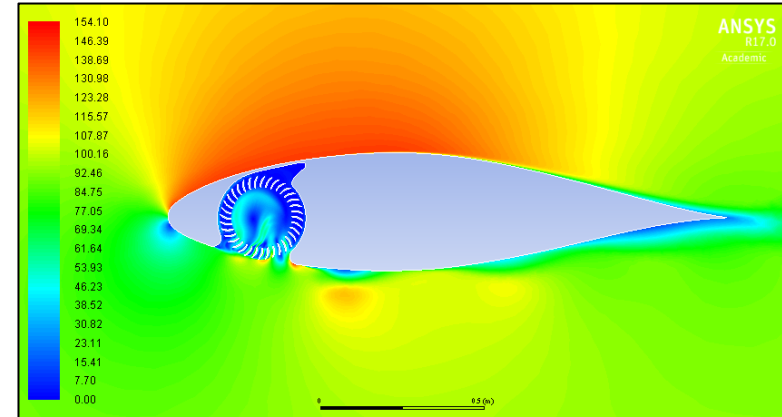


Figure A.2. Velocity contours at 4 deg AOA
($C_l=0.775$, $C_d=0.0065$)

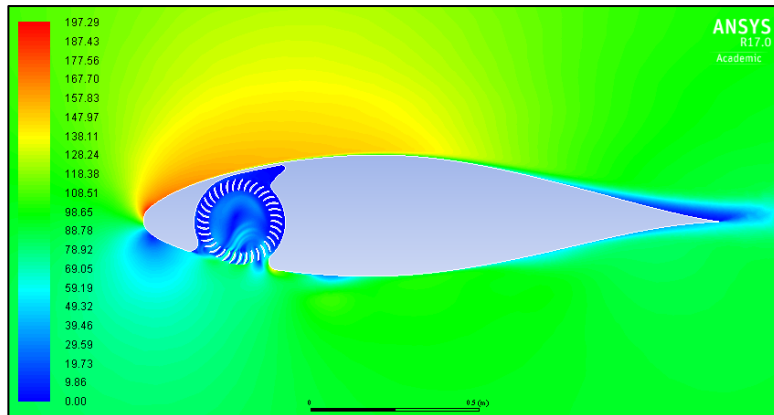


Figure A.3. Velocity contours at 8 deg AOA
($C_l=1.065$, $C_d=0.0075$)

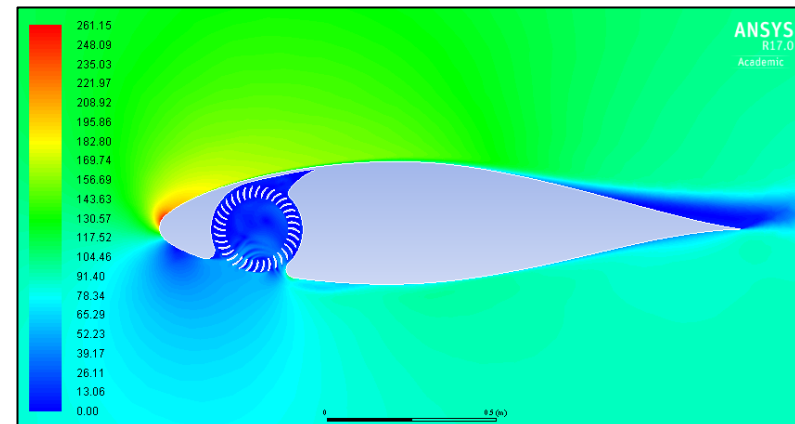


Figure A.4. Velocity contours at 12 deg AOA
($C_l=1.065$, $C_d=0.01875$)

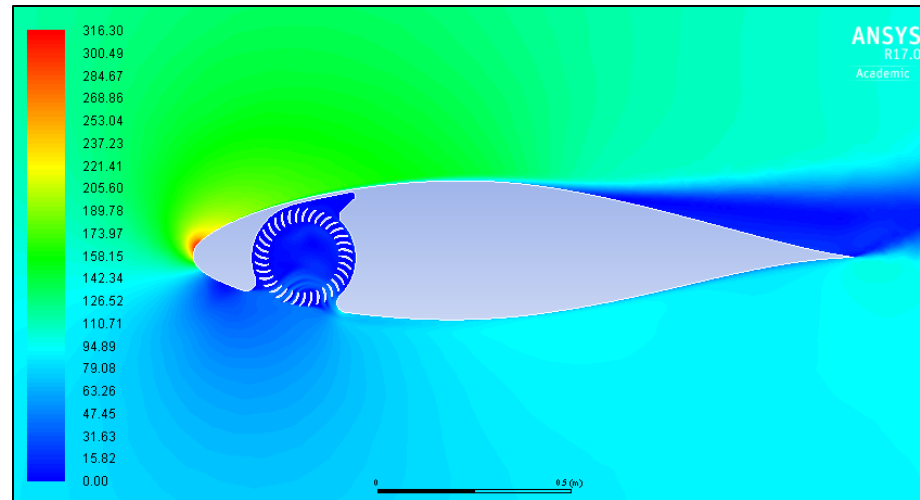


Figure A.5. Velocity contours at 16 deg AOA ($C_l=1.532$, $C_d=0.043$)

B. The CFF airfoil velocity contours at cruise

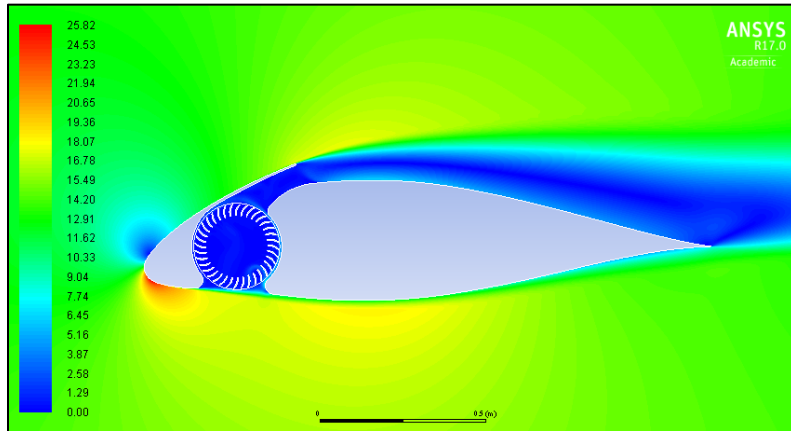


Figure B.1. Velocity contours at 0 deg AOA

($C_l = -0.3$, $C_d = 0.0278$)

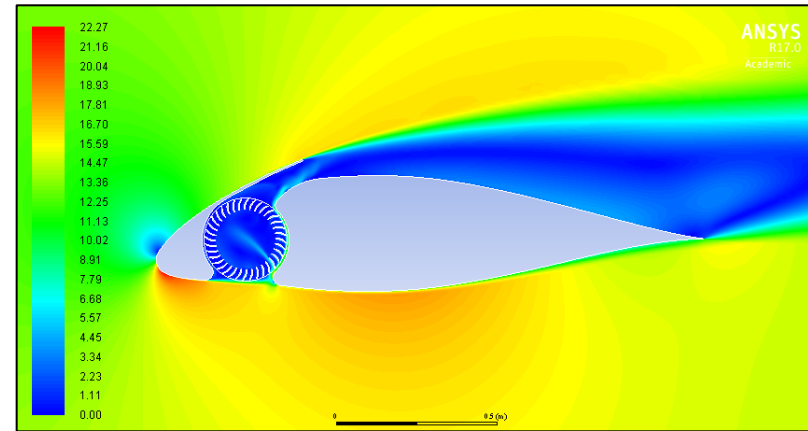


Figure B.2. Velocity contours at 4 deg AOA

($C_l = -0.204$, $C_d = 0.1$)

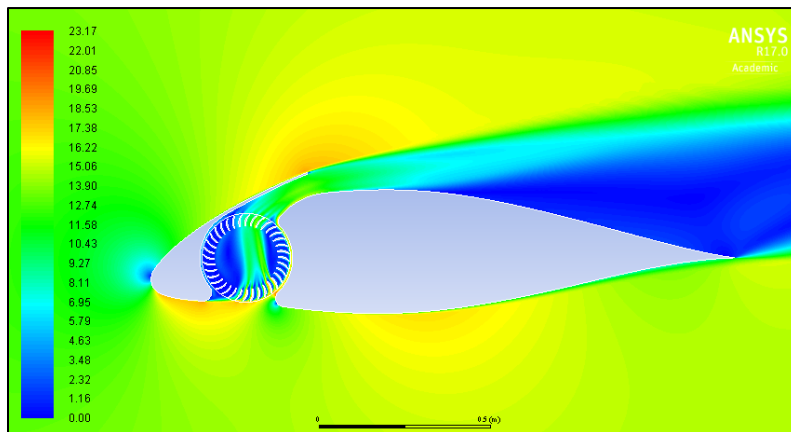


Figure B.3. Velocity contours at 8 deg AOA

($C_l = 0.028$, $C_d = 0.08$)

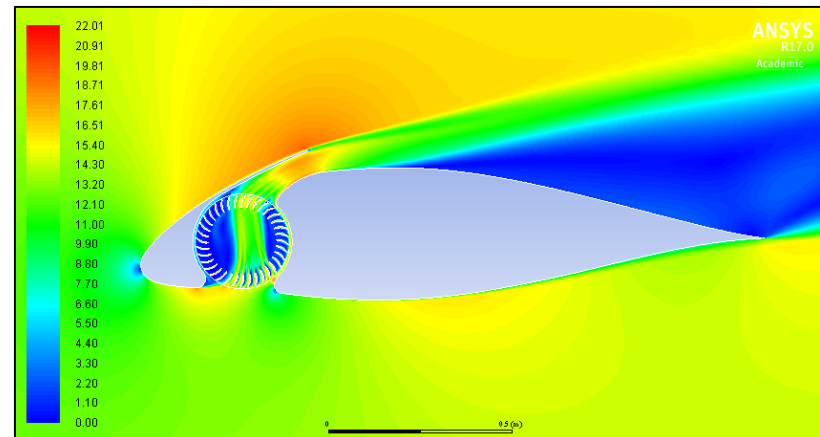


Figure B.4. Velocity contours at 12 deg AOA

($C_l = 0.335$, $C_d = 0.104$)